UNIVERSITY OF TWENTE.

MSc Thesis
Applied Physics

Iron Selenide Telluride

Thin Films and Devices

November 23, 2011

Author:
Sebastiaan Waanders

Graduation committee:
Prof. dr. ir. H. Hilgenkamp
Prof. dr. ir. A. Brinkman
dr. R. van Gastel
dr. ir. G. Koster

Thin films of iron selenide telluride ($FeSe_{1-x}Te_x$) were grown using Pulsed Laser Deposition. One film grown on LSAT exhibited superconductivity with a $T_{c,onset}$ of 9K and a $T_{c,0}$ of 5.3K. This was measured in an RT setup. The superconducting volume fraction was found to be very low, as no superconducting transition was observed in magnetization measurements. This lower than expected T_c is possibly caused by the presence of excess iron in the film, which is confirmed by the positive magnetic moment observed in magnetization measurements. The structure and stoichiometry of FeSeTe thin films was studied using X-ray diffraction, which showed clear (00l)-oriented growth of the thin film, with a good alignment on the substrate. Also, the presence of defects in the thin film was observed by comparing rocking curves of the film with those from the target crystal.

Using thin flakes of $FeSe_{0.4}Te_{0.6}$, N-S and S-I-S junctions were fabricated using conventional photolithography and liftoff. The N-S junction exhibits intermediate behavior between a fully transparent Andreev contact and a tunnel barrier, with an approximate value for the barrier height of $Z = 0.5$ and a mixing parameter for the two superconducting condensates $\alpha = 0.2$. The S-I-S junctions fabricated with niobium show clear Josephson behavior with a critical current of 5μA and an I_cR_n product of 2μV. The critical current was observed to be suppressed by the application of microwave radiation to the junction, and reappeared upon ramping the amount of microwave radiation, which is an indication of Josephson behavior.

Contents

1 Introduction

This report forms the culmination of approximately a year's worth of research into the physics and growth characteristics of iron-based superconductors, and specifically the iron chalcogenide superconductor FeSeTe, iron selenide telluride.

We will approach this material in two ways. First, the evolution of research into a certain type of material eventually calls for high quality thin films of this material to be produced, for reasons mentioned later on in this introduction. This was attempted by using single crystalline samples of the material, FeSeTe, as target material for pulsed laser deposition or laser ablation. Using this method, we attempted to grow epitaxial thin films that could be used in experiments.

In addition to the thin film growth of this iron-based superconductor, experiments were carried out on single crystalline samples on which junctions were created to investigate the order parameter symmetry of this material.

This introduction aims to give some background information on the basic concepts of superconductivity and thin film growth. Topics discussed include the theory (for as far as consensus has been reached) describing superconductivity, order parameter symmetry and possible ways to establish this, and basic principles of thin film growth.

We then continue by describing the approach and results with regard to the growth of this material, problems encountered and recommendations, followed by a chapter focused on transport measurements on normal-superconductor junctions in which we tried to establish indications towards certain order parameter symmetries in the iron chalcogenides. In addition to this, we describe the crystalline properties of the grown films as established by means of x-ray diffractometry or XRD.

1.1 Superconductivity

Approximately one hundred years ago in 1911, after his successful attempts at liquefying helium, Heike Kamerlingh Onnes in Leiden sought to verify the low-temperature behavior of the electrical resistance of metals. There was significant dispute in the time about this, and Kamerlingh Onnes was in the unique position to be able to experimentally verify the theories from (amongst others) Van der Waals and Lord Kelvin, because at the time Leiden was the only place in the world where these measurements could be carried out.

On cooling down a mercury resistor, Kamerlingh Onnes noticed that below a certain temperature, the resistance completely disappeared. (Fig. 1.1) ("Kwik nagenoeg nul", according to his lab notes) After excluding experimental errors like for example shorts in the circuit, he decided that this was a new phenomenon, and he coined it "supraconductivity" or "supraleitung"[1].

In the years after the initial discovery, more and more metals were discovered to exhibit the same behavior, at varying temperatures. After initial phenomenological theories by the London brothers and later on Ginzburg and Landau, in 1957 a trio of American scientists, Bardeen, Cooper and Schrieffer proposed the theory now known as "BCS theory", in which they offered a microscopic theory of superconductivity[2]. It accurately described the low temperature behavior of simple metals and alloys, and could predict their critical temperatures based on materials parameters like the Debye temperature, specific weight and normal state resistance.

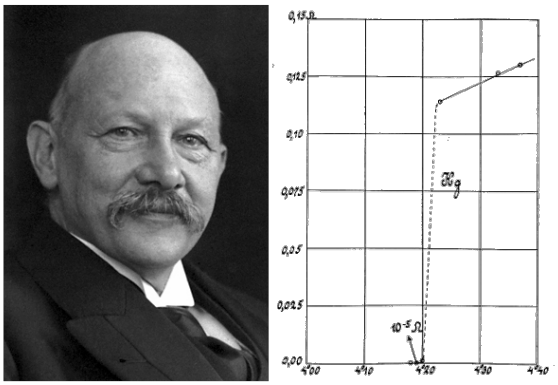

Figure 1.1: Heike Kamerlingh Onnes and the discovery of superconductivity in mercury

Cooper argued[3] that below a certain critical temperature, charge carriers in the superconductor would pair up into so-called "Cooper pairs", mediated by lattice vibrations or phonons. These *Cooper pairs*, consisting of two fermions, are of bosonic nature and as such the entire ensemble of Cooper pairs can condense into a Bose-Einstein condensate. This means they can all be described by the same wave function, which they introduced as the superconducting *order parameter*, and argued that superconductivity was a (second order) phase transition, with a complex order parameter. This order parameter Ψ, or rather its *symmetry* to be more specific, gives vital information about the exact pairing mechanism that creates the attractive potential that eventually leads to the formation of Cooper pairs.

An intuitive (but overly simplified) picture about Cooper pair formation in BCS superconductors can be drawn as follows. An electron (negatively charged) moving through a positive lattice of ions exerts an electrostatic force on these ions, causing the lattice to deform. This creates a local positive charge density, which then attracts another electron, which is now coupled to the first electron. This is schematically shown in Figure 1.2.

However, as research progressed and new superconducting materials were discovered, not all materials showed the properties predicted by BCS theory. Extensions to the BCS theory were developed, most noticeably by Eliashberg in 1960, who generalized the BCS equations for the strong-coupling limit for the electron-phonon interaction. Even the discovery of two-band superconductivity in MgB_2 could be explained using an adaptation of standard BCS theory. However, with these relatively minor adjustments

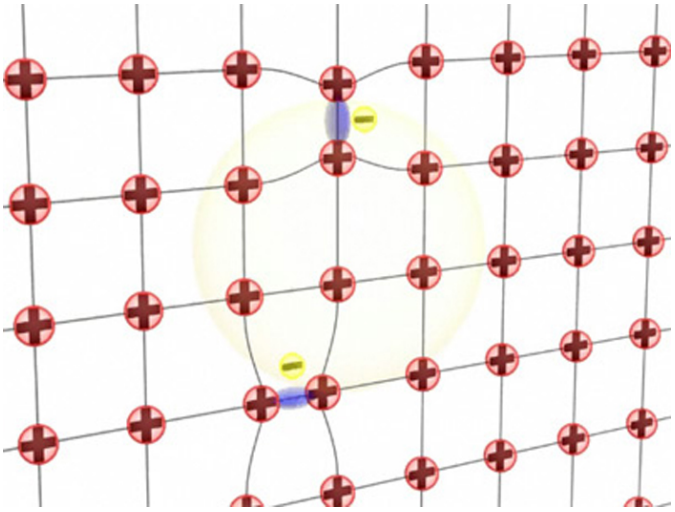

Figure 1.2: Electron-phonon Cooper pair formation. From [4]

all materials could still be described, and all was well.

All was well indeed, until in 1987 Georg Bednorz and Alex M´uller at IBM Z´urich discovered superconductivity in the perovskite material $Ba_xLa_{5-x}Cu_5O_{5(3-y)}$[5]. BCS theory had predicted, for realistic material parameters like the Debye temperature and density of state, a maximum critical temperature of approximately 30K. However, this new material exhibited a critical temperature of 35K, which was spectacular. This triggered a phenomenal research effort throughout the world, and within a few years many more of these cuprate superconductors were discovered, with a maximum T_c of 135K for the material $HgBa_2Ca_2Cu_3O_x$. Apparently a new microscopic theory for superconductivity was necessary, as these new materials proved to be quite different from the BCS-superconductors.

Charge transport in these cuprates is very much two-dimensional, in contrast with the BCS superconductors in which superconductivity is isotropic in space. Most of the superconducting physics occurs in the CuO_2 layers and CuO chains, and charge carriers are injected into them by the interstitial layers separating them. Also, the phase diagram of the cuprates shows a great richness in electronic phases, as shown in Figure 1.3. The parent compounds of these materials do not show superconductivity, but rather behave like Mott insulators and antiferromagnetism. However, upon doping the compound with electrons or holes, a superconducting dome emerges, which has a maximum for a certain doping level.

After much debate, the superconducting order parameter in the cuprates was found to be (predominantly) *d*-wave[6], in which superconductivity only occurs along the crystallographic axes of the material, and the phase of the superconducting order parameter changes between the 'lobes' of the wavefunction. However, even after thousands of research articles published in scientific literature since the discovery of high-temperature

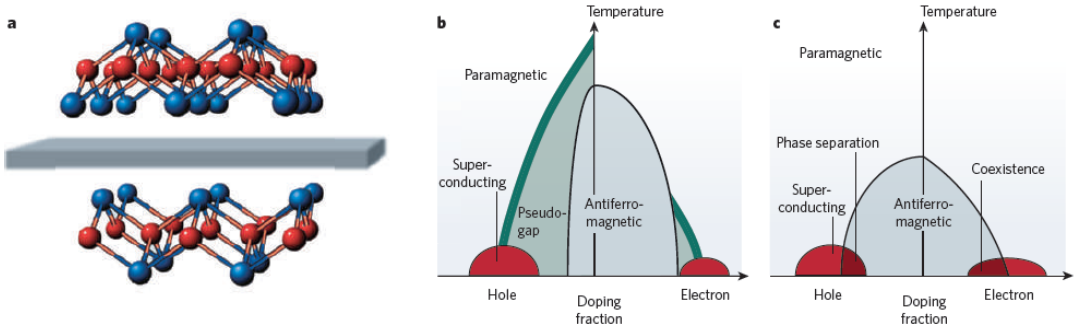

Figure 1.3: Iron-based and copper-based superconductors. (a) Generic crystal structure for the iron-based superconductors, consisting of a square lattice of iron atoms (red) with pnictogens or chalcogens (As, Se, Te, etc.) shown in blue. The grey area represents any potential filler layers, which differ for the different families. (b) Generic phase diagram for the cuprate superconductors. Magnetism is suppressed as the doping fraction is increased, and a superconducting dome appears. (c) Generic phase diagram for an iron-based superconductor of the 122-family. Doping is achieved by replacing iron atoms with for example cobalt or ruthenium, or changing the pnictogen ion.

superconductivity, no consensus has been reached on the microscopic origin of superconductivity in these materials.

Then, in 2006, Hosono *et al.*[7] discovered superconductivity (by accident) in the compound $LaO_{1-x}F_xFeAs$. This was completely unexpected, as they did not seem to resemble the properties of the BCS or cuprate superconductors. Most strikingly, the compound contains iron, a magnetic material, which is unexpected as superconductivity and magnetism were thought to be an impossible combination.

1.2 Iron-based superconductors

Discovered in 2006, the iron-based family of superconductors shook up the world of superconductivity research. After all, wasn't it Bernd Matthias[8] who stated in his famous "six rules for finding new superconductors" that one should stay away from magnetism? This discovery lead to a huge surge in research, with new superconducting materials popping up every other week, and at its peak two papers on iron-based superconductors appeared on the public servers of arXiv.org, a popular place for quick publication of (non peer-reviewed, I should add) research, *every day*.

It's interesting to draw parallels and note the differences between these new iron-based superconductors and the other families of superconductors, like the cuprates, the BCS superconductors and magnesium diboride (MgB_2), a two-band BCS-like superconductor. The main properties of these superconductor families are summarized in Figure 1.4.

Property	Conventional superconductors	Copper oxides	MgB_2	Iron-based superconductors
T_c (maximum)	<30 K	134 K	39 K	56 K
Correlation effects	None (nearly-free electrons)	Strong local electronic interaction	None (nearly-free electrons)	Long-range (non-local) magnetic correlations
Relationship to magnetism	No magnetism	Parent compounds are magnetic insulators	No magnetism	Parent compounds are magnetic metals
Order parameter	One band, same-sign *s* wave	One band, sign-changing *d* wave	Two band, same-sign *s* wave	Two band, presumably sign-changing *s* wave
Pairing interaction	Electron–phonon	Probably magnetic (no consensus)	Electron–phonon	Presumably magnetic
Dimensionality	Three dimensional	Two dimensional	Three dimensional	Variable

Figure 1.4: Comparison of the main properties of the four most important superconductor families. From [8]

Figure 1.3 shows the phase diagram of the cuprates and the iron-based superconductors side-by-side. The similarities are immediately visible, with a nonsuperconducting antiferromagnetic parent compound, in which superconductivity emerges as magnetism is suppressed. However, for the iron-based superconductors there exists a coexistence region in which both superconductivity and antiferromagnetism occur.

It is interesting to note that the iron-based superconductors seem to combine many of the properties of the other nonconventional superconductor families. It shares the multi-band structure with MgB_2, the nonconventional isotope effects which are also seen in the cuprates, and magnetism (or electron spin) seems to play a significant role in the pairing mechanism. The crystal structures of cuprates and pnictides are remarkably similar as well, with transport taking place in the copper oxygen planes in the cuprates, whereas in the iron-based superconductors transport occurs in the iron-layers. As with the cuprates, charge carriers are provided by the interlayers to the planes in which conduction occurs, although some iron-based superconductors like $FeSe_{1-x}Te_x$ do not have any interlayers and show superconductivity without doping. However, much is yet unknown about these iron-based materials, and the main point of research is aimed at the symmetry of the superconducting order parameter, which is vital in testing theories regarding the pairing mechanism in superconductors.

1.2.1 Order parameter symmetries

The superconducting order parameter Ψ is defined as

$$\Psi(\mathbf{r}) = \sqrt{n_s(\mathbf{r})}e^{i\phi(\mathbf{r})}, \tag{1.1}$$

where n_s can be seen as the number of Cooper pairs and ϕ_r is the phase of the wavefunction. For BCS-like superconductors, this order parameter is isotropic in space, meaning that superconducting energy gap has the same magnitude and phase in all directions. The cuprates however show a gap symmetry which is highly anisotropic, with lobes along the crystallographic *ab*-axes in which a phase difference exists between perpendicular lobes. This was finally proven by Tsuei and Kirtley[6] in a phase-sensitive experiment.

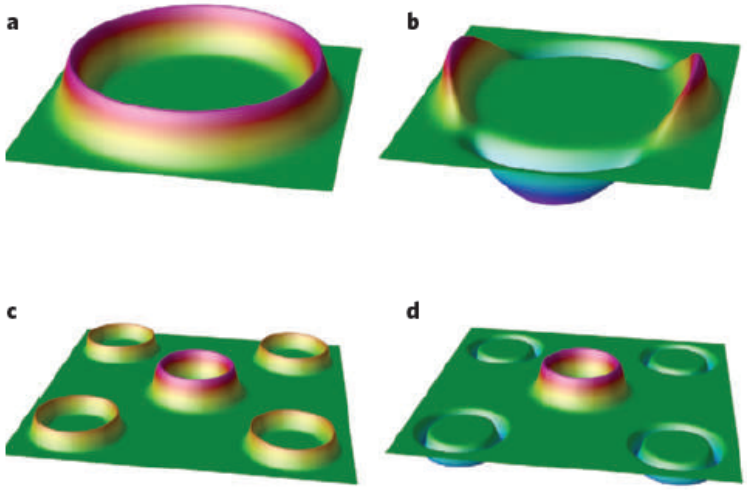

Figure 1.5: Cartoon of the order parameter symmetries of a BCS superconductor (s-wave, top left), a cuprate superconductor (d-wave, top right), MgB_2 (s_{++}, bottom left) and the iron-based superconductors (possibly $s_{\pm}$, bottom right

For the iron-based superconductors, the jury is still out. Because of the two-band nature of the order parameter, which seems to consist of two separate condensates with each showing s-wave like behavior, the traditional phase-sensitive experiments that clarified the issue in the cuprates are not applicable in this situation. Figure 1.5 shows a schematic representation of the order parameter symmetries for the four main families of superconductors.

Most strikingly, the Fermi surface of the iron-based superconductors is likely composed of different surfaces, with a π phase difference between the two bands. Moreover, the different Fermi surfaces can be matched by a process called *nesting*, which is the translation of a Fermi surface by a suitable momentum vector. This is thought to be facilitated by a spin-density-wave present in many iron-based superconductors, and leads to the suspicion that Cooper pair formation in these materials is mediated by spin-interactions[9].

1.2.2 Experimental verification of the order parameter symmetry in iron-based superconductors

As described by Van Harlingen in 1995[10], methods of determining the superconducting order parameter symmetry fall into two categories: experiments which measure the *magnitude* of the order parameter and experiments which measure the *phase* relation of the order parameter. An example of the first category is angle-resolved photoelectron spectroscopy or ARPES, which basically maps the Fermi surface of the material. However, this technique can only make a clear distinction between s-wave and d-wave symmetry by detecting nodes in the gap function. It is clear that only ARPES measure-

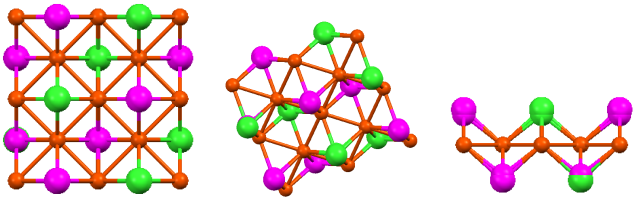

(a) (b) (c)

Figure 1.6: The crystal structure of iron selenide telluride. Iron atoms in orange, selenium atoms in pink, tellurium atoms in green.

ments can never tell the whole story here, so we will need a phase-sensitive experiment to undoubtedly confirm the order parameter symmetry.

One way to measure the phase of the order parameter symmetry is Josephson interferometry. These kinds of experiments, amongst which are the well-known corner-junction, tricrystal and π-ring experiments[6, 11] established the d-wave symmetry in the cuprates. Until now, very few phase-sensitive experiments have been conducted on the iron-based superconductors, and they have not given the ultimate proof of either d- or s-wave symmetry[12].

In an article on the arXiv preprint server, Parker and Mazin[13] propose a few possible phase-sensitive tests of the pairing symmetry in the iron-based superconductors. Their idea is to take advantage of the difference in tunneling probabilities for hole-like and electron-like quasiparticles through barrier structures of variable thickness.

Another article proposes a different kind of experiment, in which the two-band nature of the iron-based superconductors shows itself in normal metal - superconductor junctions in the conductance[14]. If a phase shift of π is present between the two bands of the iron superconductor, they will result in Andreev bound states at nonzero energy. The presence of these bound states within the gap would be strong evidence for $s_{\pm}$ symmetry.

If these two scenarios are to be tested, we need to be able to create both NS and S-I-S junctions on these materials. So far, very few high quality junctions have been realized, and none yet on the material of our choice, $FeSe_{1-x}Te_x$.

1.2.3 Iron Selenide Telluride

Iron selenide (FeSe), is the simplest iron-based superconductor, from a crystallographic point of view. Only the iron-chalcogen layers are present in this compound, without any interlayers. It exhibits superconductivity at 8K[15], which can be improved by substitution of selenium ions with tellurium. The optimal stoichiometry of this compound is $FeSe_{0.5}Te_{0.5}$, with a T_c of 17K reported in thin films[16].

The FeSeTe superconductor is a remarkable material. One of the parent compounds,

FeSe, is an intrinsic superconductor, whereas the other, FeTe, is a semiconductor and exhibits antiferromagnet ordering[17]. A good overview of the physics of FeSeTe can be found in the article by Mizuguchi[18]. Both parent components have a PbO crystal structure, and the resulting superconductor $FeSe_{1-x}Te_x$ also shows this crystal symmetry. The increase in T_c when FeSe is combined with FeTe is thought to be caused by the stronger antiferromagnetic fluctuations present in FeTe[19].

Good quality superconducting crystals have been grown for both $FeSe_{1-x}Te_x$ and FeSe, and a number of groups have reported thin films grown of this material by laser ablation. This will be discussed in the chapter on film growth. Wu *et al*[20] made the only reported junctions on $FeSe_{1-x}Te_x$, by depositing a thin film of the material on a niobium-doped STO substrate. From the resulting current-voltage characteristic of this semiconductor-superconductor junction they estimate the superconducting energy gap to be approximately 2.06meV at 4.2K.

By growing thin films of $FeSe_{1-x}Te_x$ and creating the first Josephson and N-S devices of this material we hope to pave the way for further experiments that can elucidate the order parameter symmetry of this remarkable material.

2 Junctions on $FeSe_{0.4}Te_{0.6}$ crystals

To study the properties of these new iron-based superconductors, transport measurements were carried out on devices made with thin flakes of iron selenide telluride. Different devices were manufactured, combining the flakes with normal- and superconducting materials to study the properties of hybrid junctions. In this chapter, we will review the physics of tunneling effects, the different types of junctions that are studied and describe the process involved with manufacturing these devices, as well as the result from transport measurements on these devices.

2.1 Junctions with superconductors: the tunneling phenomenon

The phenomenon of particle tunneling is one of the many extraordinary effects that occur because of the quantum mechanical nature of electronic transport. Consider two metals separated from each other by a thin layer of insulating material, typically of the order of nanometers. Classically, electron transport through the insulating barrier is prohibited when the energy of the electron is lower than the height of the insulating barrier. However, due to the wavelike nature of the electrons, there is a finite possibility for the charge carrier to penetrate the insulator, passing to the other metal lead. This process is known as *tunneling*, and forms the basis of everything we are about to discuss.

For normal metals, the behavior of a tunnel junction is ohmic at low voltages, but as soon as one or both of the leads consist of superconducting material, things change. In the next few sections, we will discuss these effects, first discovered by Giaever in 1960 and Josephson in 1962, respectively[21, 22].

2.1.1 Normal metal - superconductor junctions

The phenomenon of electrical transport from a normal metal to a superconductor has been widely studied. The behavior of such a normal-superconductor (N-S) junction has been described by Blonder, Tinkham and Klapwijk[23].

Consider an electron incident on a normal metal-superconductor interface. The strength of the barrier at the interface Z is modeled by a repulsive potential at the interface:

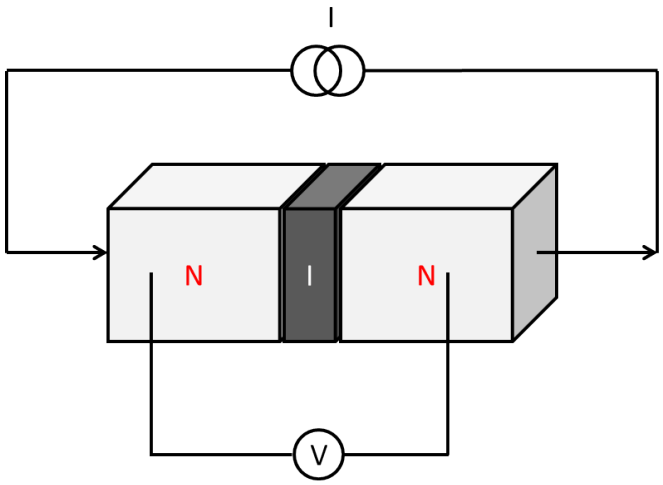

Figure 2.1: Schematic representation of a normal metal - normal metal tunnel junction

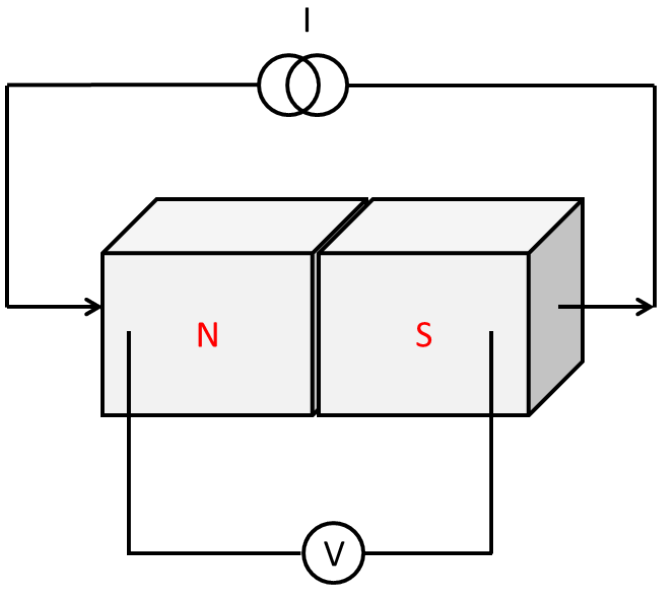

Figure 2.2: Schematic representation of a normal metal - superconductor junction

$$Z = \frac{U_0}{\hbar \nu_F}, \tag{2.1}$$

where U_0 is the height of the barrier, and ν_F the Fermi velocity of the incoming electron.

The existence of a gap in the energy spectrum of a superconductor gives rise to different transport regimes. Depending on the energy of the electron and the strength of the insulating barrier separating the metal and superconductor, there are four possible actions for the electron incident on the interface.

- The electron can reflect back into the normal metal, for a non-transparent barrier. This probability increases with Z.
- For $E < \Delta$, because there are no electronic states available in the superconductor below the gap, the electron will retroreflect as a hole in the normal metal, leaving a Cooper pair in the superconductor. This process is known as *Andreev reflection*, and its probability is small for energies higher than the superconducting gap Δ, and goes inversely with the strength of the barrier for sub-gap energies.
- For $E > \Delta$, the electron can tunnel through the superconductor as a quasiparticle. This probability is zero for energies lower than the gap energy, and decreases with increasing Z for $E > \Delta$.
- For $E > \Delta$, the electron can tunnel with branch crossing. The probability of this event occurring is very small, both below and above the gap energy.

Depending on the strength of the insulating barrier and the energy of the electron, the amplitudes of these processes will vary. For energies below the superconducting gap, tunneling is not permitted, as no electronic states are available in the superconductor at these energies. The electron is then left with two options: either reflect off the barrier, or retroreflect as a hole, which leaves a Cooper pair in the superconductor.

The normalized conductance of such a junction is shown in Figure 2.3 for various values of the barrier parameter Z. It is immediately clear that Andreev reflection causes an increase in the conductance of the junction for energies below the gap. When Z is increased, eventually the result from a normal NIS junction is obtained, which makes sense, as it represents a perfectly insulating barrier.

For a normal s-wave superconductor, the conductance of such a junction is shown in Figure 2.3.

Of course, the normal BTK model makes a few assumptions in its derivation, i.e.

- Finite temperature is not taken into account. However, this is easily solved by convolving the result from BTK with the Fermi function at the temperature of interest.
- The barrier is ideal, without pinholes and inhomogeneities so we can define one single value for Z.

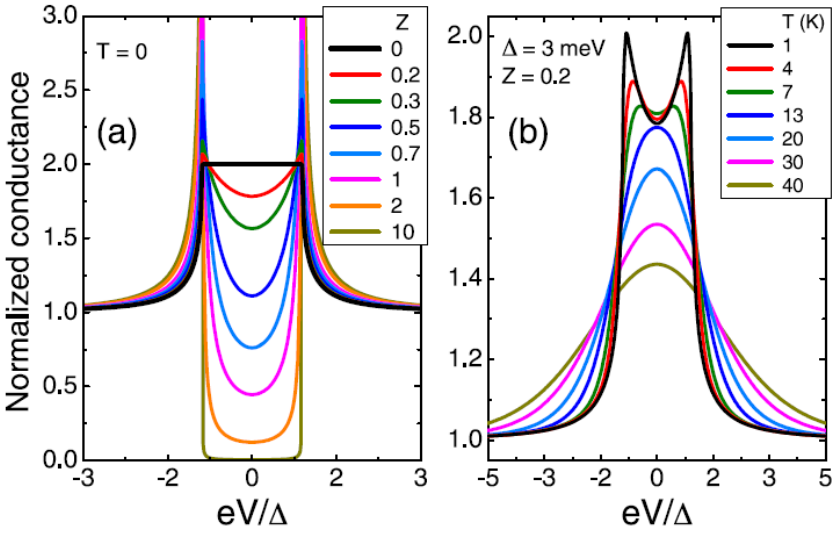

Figure 2.3: Left: normalized conductance curves at $T = 0$ as a function of the barrier parameter Z. Right: effect of nonzero temperature for fixed gap energy and barrier strength. From [24]

- The model is purely 1-dimensional, assuming current transport only perpendicular to the junction interface
- The superconducting wave function is assumed to be homogeneous and isotropic in space (i.e. *s*-wave)

The last assumption is quite interesting. It has been shown ([14, 24, 25]) that deviations from ideal s-wave symmetry in the superconductor gives rise to a plethora of fascinating effects, like zero-bias conductance peaks[25]. Also, the supposedly multiband nature of the iron-based superconductors has profound influence on the behavior of NS-junctions. This was shown in an article by Golubov *et al.*[14], who derive Andreev spectra for the case of a junction in the *ab*-plane of a two-band superconductor. They noticed a profound difference between the tunneling spectra for an s_{++} order parameter symmetry and an $s_{\pm}$ order parameter symmetry. Where for the case of an s_{++} order parameter a zero-bias anomaly exists for high-transparency contacts ($Z = 0$), destructive interference between the two bands in the $s_{\pm}$ case leads to the disappearance of this feature. Additionally, in the tunneling regime ($Z \gg 1$) bound states at nonzero energy appear, as shown in Figure 2.4. These bound states are not present in the case for s_{++} order parameter symmetry.

2.1.2 Superconductor - insulator - superconductor junctions

First described by Brian Josephson[22], the electrical transport through a superconductor-insulator-superconductor junction shows distinctly different features compared to a nor-

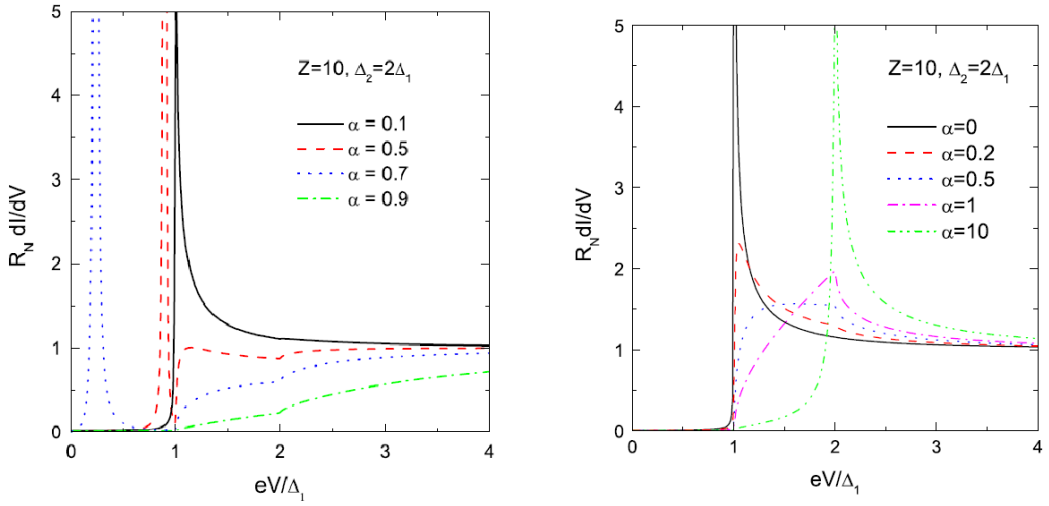

(a) $s_{\pm}$ **(b)** s_{++}

Figure 2.4: Conductance in the tunneling regime, Z=10 for $s_{\pm}$ and s_{++} order parameter symmetry. Taken from [14].

mal tunneling junction, due to the long-distance coherence of the superconducting order parameter and the fact that charge carriers in a superconductor consist of bound states of two electrons, known as *Cooper pairs*.

The so-called Josephson effects arise when two superconductors are weakly coupled, for example by separating them by a thin insulating barrier. In the absense of a magnetic vector potential $\mathbf{A}$, the current that flows through the junction is determined by the phase difference of the two superconducting condensates:

$$I_s = I_c \sin(\theta_1 - \theta_2) = I_c \sin\phi, \tag{2.2}$$

where $\phi = \theta_1 - \theta_2$ is the phase difference between the two superconductors. The current-voltage characteristic of such a Josephson junction is distinctly nonlinear, with no quasiparticle tunneling occuring for bias voltages lower than the gap energy of the superconductor. However, Cooper pairs can tunnel through the barrier, this current is called the *Josephson supercurrent*, which has a maximum value I_c. When the current through the junction exceeds this critical current I_c, the junction goes to the so-called voltage state, and a voltage arises over the junction.

The value of this critical current is determined by the gap energy of the superconductor and the resistance of the junction, and decreases with temperature:

$$I_c = \frac{\pi\Delta(T)}{2eR_n}\frac{\tanh(2\Delta(T))}{2k_bT} \tag{2.3}$$

The immediate consequence of this relation is the observation that for a good quality junction, the product of I_c and R_n should be of the order of the superconducting gap.

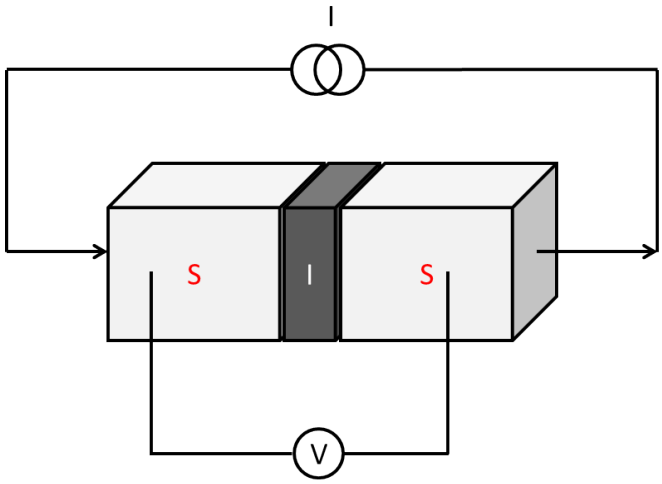

Figure 2.5: Schematic representation of a superconductor - insulator - superconductor junction

However, junction quality can vary depending on the production process, materials used, quality of the insulating barrier et cetera. This will often lead to a decrease in the critical current of the junction.

In order to evaluate if a true Josephson junction has been fabricated, a couple of properties of the junction can be tested. First, the phase difference between the superconductors does not only depend on the values of the phases themselves, but should be generalized to include the effect of a magnetic vector potential. This *gauge invariant phase difference* γ is given by[26]

$$\gamma = \phi_2 - \phi_1 - \frac{2e}{h}\int_1^2 \mathbf{A}\cdot d\mathbf{l} \tag{2.4}$$

Taking this effect into account, it can easily be shown[26] that the critical current of a Josephson junction will vary as a function of the applied magnetic field perpendicular to the junction:

$$I_c = I_c(0)\left|\frac{\sin\left(\pi\Phi/\Phi_0\right)}{\pi\Phi/\Phi_0}\right|, \tag{2.5}$$

where Φ is the flux threading the junction and Φ_0 represents the elementary flux quantum ($2\times10^{-15}\mathrm{Tm}^2$). The pattern resulting from this effect is known as a *Fraunhofer pattern*. It should be noted that the description given above is valid only for s-wave superconductors, and deviations from this predicted critical current modulation are a sign of order parameter symmetries other than s-wave[27].

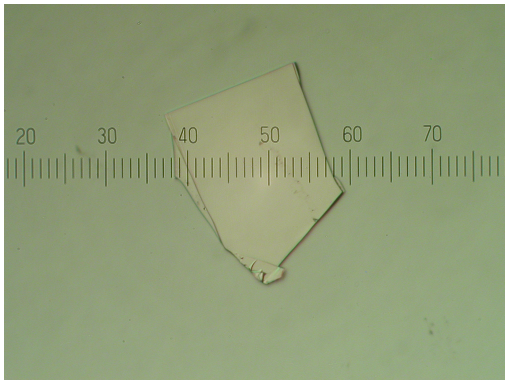

(a) Bare FeSeTe flake. The size of the flake is approximately $60 \times 40\mu$m

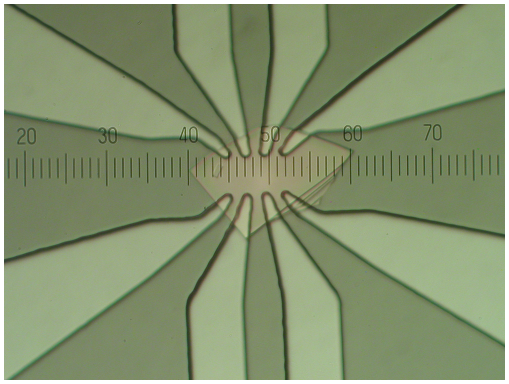

(b) Flake with photoresist structure. Metal deposited in the light areas will remain on the device after lift-off of the photoresist.

Figure 2.6: FeSeTe flakes on Si(100)

2.2 Junction fabrication

A series of junctions was made on thin crystal flakes of iron selenide telluride ($FeSe_{0.4}Te_{0.6}$), provided by the University of Amsterdam, using a micromechanical cleaving process better known as the "Scotch tape method", made famous by the discovery of graphene[28]. Crystals were cleaved with pieces of scotch tape and subsequently deposited on 10×10mm Si(001) and SiO_2 substrates. Initial junctions were fabricated on Si(001) substrates, but after more experiments it turned out depositing the flakes on silicon dioxide substrates yielded more and higher quality flakes, of varying thickness. This enabled us to select suitable crystal flakes for device manufacturing. Requirements for a good flake were smooth surface morphology and sharp, clean edges. Flakes of different thickness were visible, and this method seems to be a very good approach towards device manufacturing. The crystals cleave very easily and yield both large and small flakes, ranging in size from 5 to $100\mu m$. An example flake is shown in Figure 2.6a.

The substrates with flakes were subsequently covered by a layer of Olin 907/17 photoresist which was baked out for 60 seconds at 100°C. This step enables us to define a structure in the photoresist using UV photolithography, which after developing results in a structure as shown in Figure 2.6b.

Then niobium or aluminum was deposited using a DC sputtering step, which after lifting off the remaining photoresist with acetone results in our device. 200nm of metal was deposited on the structures, which proved enough to cover the edges of the flake and most structure features ended up in the final device. Some intended features did not survive the lift-off process, resulting in approximately one in four arms of the structure not ending up in the final device. This was accounted for in the original design of the structure, as multiple leads going up the flake ensured good redundancy.

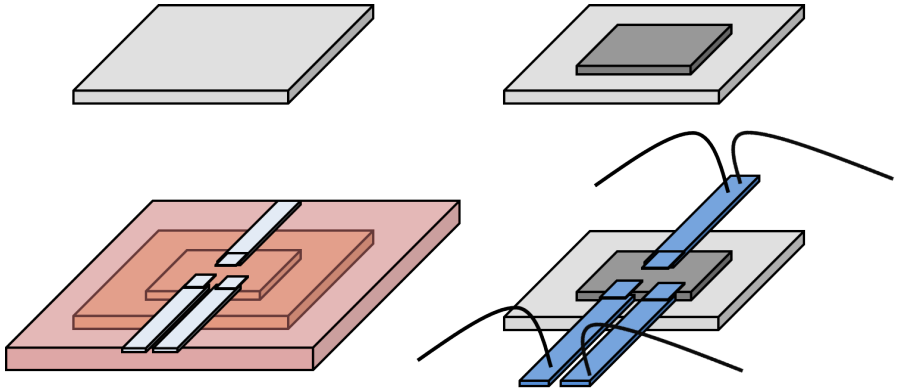

Figure 2.7: Step-by-step illustration of the manufacturing process of an FST junction. Top left: bare substrate. Top right: flake on substrate. Bottom left: structure defined using photoresist (pink). Bottom right: niobium structure with bond wires, after lift-off.

2.3 Niobium - FeSeTe junctions

Niobium - FeSeTe Josephson junctions were fabricated by the method described above, and were analyzed in the bath cryostat in our lab. IV-curves were measured by placing aluminum bond wires on the bond pads connected to the niobium leads. Two bond wires were placed on the first electrode, and one each on two other electrode, so effectively the interface between the niobium on the first electrode and the FST superconductor is measured in a quasi-four point geometry. This means that the voltage contact on lead 3 draws no current, and no contact resistances are measured, leaving just the resistance of the junction.

The IV behavior of such a junction is shown in Figure 2.8, and was verified for two other junctions. These IV characteristics were measured by applying a current through the junction and measuring the voltage response. The current applied was a triangular waveform with a maximum value of 20μA. Both voltage and current were measured by a National Instruments PXI board, with a pre-amplifier to improve resolution. Multiple current sweeps were executed, and no hysteresis effects were observed.

The critical current of the junctions was very low, in the order of 5 μA, which combined with the normal state resistance of 5Ω results in an I_cR_n product which is significantly lower than expected, in the order of microvolts. For a good quality Josephson junction, this product is of the order of the superconducting gap, which is expected to be around 5 mV. This means our junction is far from good, but this was to be expected as barrier control was virtually nonexistent. The residual oxide on top of the iron selenide telluride flake has not been removed by an etching step before depositing niobium, and acts as the barrier between the two superconductors. This residual oxide is uncontrolled, and therefore it is to be expected that the actual junction might be comprised of several tiny junctions, yielding a bad contact.

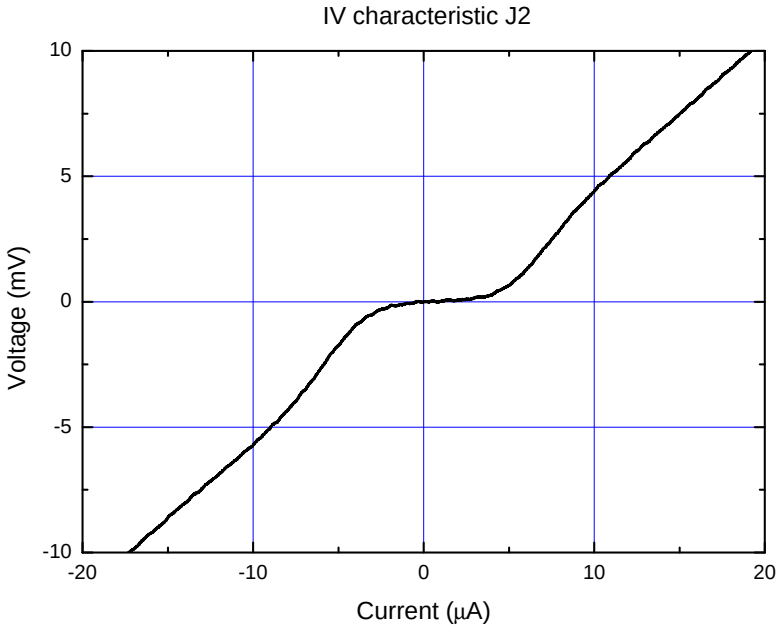

Figure 2.8: Current-voltage characteristic of a hybrid niobium - FeSeTe junction

In ideal circumstances, one would etch residual contaminations from the iron selenide telluride flake, subsequently deposit a couple of Ångstroms worth of insulating material (for example, aluminum oxide) and then proceed with depositing the niobium electrode. This would most likely result in a better defined insulating barrier and I would expect it to strongly enhance the I_cR_n product of the junctions.

The low critical current of the junction means that the signal-to-noise ratio or SNR in our measurements is quite low, as our measurement equipment has an inherent noise which is of the order of 1μV.

The superconducting state is clearly visible as no voltage is measured from -5 to +5 μA, and subsequently a transition to the normal state is visible for both positive and negative bias currents. Significant attention should be paid to the fact that the these junctions are (predominantly) c-axis oriented. Contrary to the cuprate superconductors, which are two-dimensional in nature and have very little if any c-axis conductivity, these junctions show clear signs of c-axis transport, which is bad news for anyone advocating d-wave order parameter symmetries in these systems.

A magnetic field was applied to the junctions to test for the occurance of a Fraunhofer pattern in the critical current as function of magnetic field. However, due to problems with one of the amplifiers used to measure the voltage over the junction, the dataset of this measurement was corrupted. Because the junction's performance had decreased significantly (i.e. no supercurrent was observed after cooling down again), the measurement

could not be repeated. However, we did observe a modulation of the critical current in the junction, which disappeared upon ramping the magnetic field, and reappeared when ramping further. This is a good indication that a Fraunhofer pattern can indeed be measured on these junctions. Also, the critical current of the junction disappeared upon irradiation of the junction with microwaves, however no Shapiro steps were measured in the current-voltage characteristics of the junction.

It is interesting to note that there have been no reports in literature about this kind of hybrid S-I-S junction on the (11)-family of iron-based superconductors, so these are a world-first. A good overview on the junction experiments that have been conducted on the iron-based superconductors can be found in the review articles by Seidel[27] and Hiramatsu[29].

2.3.1 *ab*-plane contributions to conductivity

In the previous paragraph, we discussed a hybrid niobium-FST junction, which showed clear Josephson characteristics. The flake used to produce this device was about 2μm thick. Another device was created using a much thinner flake, about 500nm thick. This device did not show the expected S-I-S behavior, but rather looked like a normal metal - superconductor junction, with the gap of niobium clearly visible at about 9meV. Using the same niobium contacts, a four-point probe RT measurement was done on the junction, and it proved to show very insulating behavior. So insulating that it could not be accurately measured. This could have two reasons. Decreasing the thickness of the flake decreases the *ab*-contribution to the supercurrent in the device. Given the fact that our junction area is 2μm^2, a niobium lead of 20μm wide against a 2μm thick flake potentially makes a very large extra junction area, which possibly contributes to the total supercurrent measured in these devices. If the flake is made much thinner, the *ab*-junction area decreases with it, and the contribution of this area to the total electrical transport through the junction decreases. However, it has also been reported in literature[15], that thin films of this material seem to have a certain "critical thickness" before superconductivity arises. This could well be the case here. Otherwise, it shows that *c*-axis oriented junctions do not carry a significant supercurrent.

If *ab*-transport is significantly present in the junction characteristics as shown in Figure 2.8, then it should be possible to suppress this by applying a field perpendicular to the *ab*-plane of the flake. This was done, and very little critical current modulation was observed. This leads us to the conclusion that *ab*-transport is not significantly present in the realized junction.

A good improvement on the current junction design which could shed light on this issue would be to cover the edges of the FST flake with an insulating layer, leaving only the top surface of the flake exposed to the niobium leads. This way, only *c*-axis transport is possible, and any *ab*-contribution should disappear.

2.4 Aluminum - FeSeTe junctions

Bound states within the superconducting gap of iron selenide telluride superconductors have been argued to provide strong evidence of $s^{\pm}$ order parameter symmetry, because of interference of the two superconducting wave functions coexisting within the iron superconductor[14]. For a fully transparent interface, an Andreev contact exists. Contrary to the case of cuprate superconductors, where experiments indicate strong evidence of zero-bias conductance peaks in the dI/dV spectrum, destructive interference between the coexisting superconducting wave functions in the pnictide and chalcogenide superconductors causes this zero-bias conductance peak to disappear completely.

However, fully transparent interfaces ($Z \ll 1$) are very hard to fabricate in a controlled way, and measuring them is not straightforward because of the inherently low interface resistance. In the same paper, Golubov *et al.*[14] argue that for large values of Z ($Z \gg 1$), the junction is in the tunneling limit, and the two-band nature of the iron superconductors gives rise to Andreev bound states that exist in the gap at finite bias voltages. The existence of such bound states are strong evidence for a π phase shift between the two condensates, and experimental evidence for them could provide the sought-after "smoking gun". Should the order parameter symmetry be s_{++}, there will be no bound states at finite bias voltage, even though band interference does occur, resulting in a complex dI/dV characteristic.

A normal metal - superconductor junction was fabricated by sputter depositing 200nm thick aluminum leads on a FeSeTe single crystal flake on a silicon dioxide (SiO_2) substrate. The IV characteristic of this junction was measured in a quasi-four point method at 1.8K, after which a conductance curve was obtained by numerically differentiating. This conductance plot is shown in Figure 2.9. Clearly visible is a maximum for approximately 3meV, which corresponds well to the values found in literature for $FeSe_{1-x}Te_x$[30]. Another shoulder in the curve is visible at -9meV, which could possibly point at a second gap feature, corresponding to the second gap of the (multiband) $FeSe_{1-x}Te_x$. These features are stable over time, measured at different days, after thermal cycling. This indicates that these junctions are rather stable and do not degrade over a period of multiple days. However, due to the fact that one of the leads was destroyed by applying too high a current through the sample, no further measurements at different temperatures could be measured, which would be interesting to determine the behavior of the system at different temperatures. The resistance of this junction is 1.1kΩ. It's interesting to note that the conductance of the junction does not completely go back to the "normal" state, only for very high bias voltages.

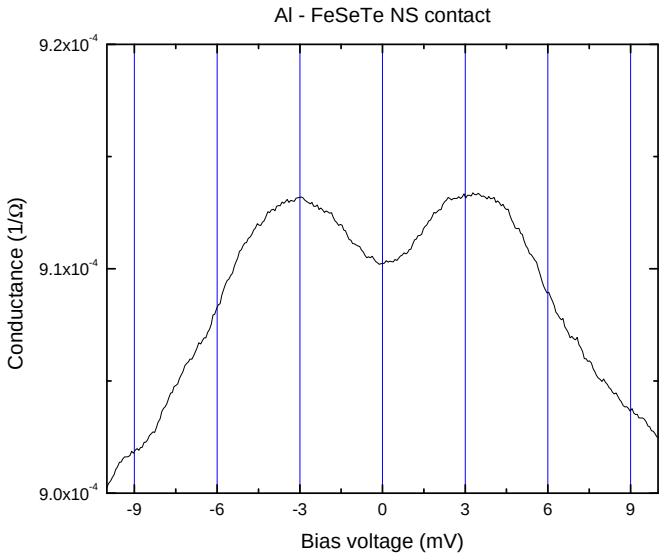

Figure 2.9: Conductance of an aluminum - FeSeTe junction showing a broad, symmetric gap feature and a resistance of 1.1kΩ.

3 $FeSe_{1-x}Te_x$ thin films

After the initial discovery of a certain new material, whether it is a dielectric, perovskite or a superconductor, at some point researchers start looking for thin films of these materials. Obviously, since thin films enable researchers to create hybrid devices incorporating these new materials, enabling them to study all different properties in detail, and in a more controlled manner than single-crystals offer them. Ideally, we would like to make thin films, such that we can use them to fabricate (superconducting) tunneljunctions with them.

My criteria for a good thin film can be summarized as follows:

- High quality single-crystalline films, offering good electronical properties, if possible exceeding those of the parent (bulk) compound. For example, strain effects sometimes enhance the critical temperature T_c of superconducting thin films compared to their bulk values.
- Good morphology, and most importantly low surface roughness, in the order of $1-2$nm RMS.
- Isotropic films, without any composition gradients.
- Well defined growth process, enabling researchers to grow films of arbitrary thickness.

This means that in order to grow good films of iron selenide telluride, we need a good understanding of the crystal (structure, bulk properties), the growth process and the parameters that influence thin film quality. Multiple tools were used to gain insight in these processes in this research project. First, basic electronic properties like the evolution of electrical resistance as a function of temperature were studied in a dipping cryostat. Here we measure the resistivity of the film in a four-point or Van der Pauw-configuration at different temperatures. This enables us to measure the transition from the normal state to the superconducting state, in the same way Kamerlingh Onnes did it in 1911, albeit with slightly newer equipment.

Secondly, the structural properties of the deposited films were studied using an X-ray diffractometer or XRD. Multiple experiments were carried out using X-ray diffraction to determine the lattice parameters and orientation of the films. Also, rocking curves and ϕ-scans were measured to study the possible existence of different orientations (twinning) and defects that could negatively influence the properties of the film.

Finally, samples were analyzed using a vibrating sample magnetometer (Quantum Design PPMS/VSM), which was used to determine the magnetic susceptibilities of the films. This could give insight in the magnetic properties of the grown films, and shed light on the question if any superconducting phases are present in the films.

In this chapter we describe the growth and subsequent analysis of iron selenide telluride thin films. All films were grown in a ultrahigh vacuum pulsed laser deposition chamber and analyzed *ex situ*.

3.1 $FeSe_{1-x}Te_x$ thin films in literature

A few other groups have reported epitaxial thin films of iron selenide telluride with varying quality[29]. Their results report a wide range of deposition parameters, sometimes contradictory. One of the goals in this project was to clarify (for as much as possible) what the optimal deposition conditions for this material are, and what the influence of the different variables is on the quality of the deposited films.

Especially the Bellingieri group have shown excellent quality thin films of FeSeTe on multiple substrates[31, 16], and their success seems to be caused by the significantly shorter target-substrate distances they employ. In PLD, usually the substrate is placed at the "edge" of the plasma plume, which is the optimal position for stoichiometric growth, as most of the ablated material then nucleates on the substrate. Unfortunately, our system layout limits the target-substrate distance to 45mm, which potentially hampers the optimal growth of iron selenide telluride thin films.

3.2 Substrate choice

A first step in growing films of any material is the choice of substrate which will act as the "template" on which the thin film will nucleate. Ideally, one chooses a substrate which has a close lattice match with the material that will be grown. In our situation, three different options were available. From literature it is known that it is possible to grow superconducting thin films of iron selenide telluride on strontium titanate ($SrTiO_3$), magnesium oxide (MgO) and LSAT ($(La_{0.3}Sr_{0.7})$ $(Al_{0.65}Ta_{0.35})O_3$) substrates[31, 16, 32, 33]. An important characteristic that should be shared by both the film and the substrate is the in-plane lattice parameter. A closely matching lattice parameter is required for the thin film to grow nicely out of the substrate, using the substrate as a template for crystal growth. Both strontium titanate or STO and LSAT have very close lattice matches with iron selenide telluride: the lattice parameters a for these materials are 3.905Åand 3.868Å, respectively. Compared to the bulk in-plane lattice parameter (3.79Å) for $FeSe_{0.5}Te_{0.5}$, which is the optimally doped configuration for the material, these are very close lattice matches. However, STO has the disadvantage from a device fabrication point of view, that it can become conducting when structures are defined in

it using argon etching, a popular step in device manufacturing. Therefore, LSAT was chosen as substrate material of choice. It is a compound structure which has a cubic symmetry, similar to MgO and STO, and an insulator. A few films were grown on MgO as well, but as varying substrate material introduces yet another variable that could possibly influence our parameter survey, I decided to stick to LSAT for the rest of this project.

3.3 Thin film growth

Thin films were grown on LSAT substrates at different deposition temperatures ranging from 400 to 600 degrees Celsius using pulsed laser deposition (PLD) with a krypton fluoride (KrF) laser at 248nm wavelength. These temperatures are chosen because at higher temperatures, very rough film growth is reported in literature [33], and the best thin films seem to be grown at these temperatures. This can be understood by the fact that a certain amount of energy is needed for the impinging ions on the surface of the substrate to assemble a crystalline layer, and heating the substrate provides this energy. However, an excess of heat on the substrate might cause desorption of the ablated material from the substrate, destroying film stoichiometry. As mentioned in section 3.1, increasing the substrate temperature causes roughening of the surface of the film, which is an undesired effect. Therefore, substrate temperatures should be kept as low as possible, whilst still allowing for crystalline growth to occur.

In this process, a KrF excimer laser ablates material from a target of known composition (stoichiometry), which creates a plasma plume containing the ablated material. A substrate opposite to the target is heated to a certain temperature and material from the plume nucleates on the substrate. A schematic of the PLD process is shown in Figure 3.1. The target material is a (001)-oriented single-crystalline sample of $FeSe_{0.4}Te_{0.6}$, which was kindly provided by the Quantum Electron Matter group at the University of Amsterdam. XRD scans of the target material confirm the good stoichiometry and single-crystalline properties of the target material, as illustrated in Figure 3.9. The slightly off-optimal stoichiometry of the target was chosen as after first attempts at growing films using a target material consisting of $FeSe_{0.5}Te_{0.5}$, grown films seemed to lack in tellurium content, so extra tellurium was added to the target material to improve the stoichiometry of the deposited films.

In the beginning of this project, which overlaps with another MSc project just before the project described in this thesis[34], a nearly superconducting thin film was grown on a magnesium oxide (MgO) substrate, exhibiting a very broad transition to the superconducting state, with a $T_{c,onset}$ of 8K, whereas a superconducting transition temperature of 14K was expected, which is the T_c of the crystal. (Fig 3.3) Also, it should be noted that the film's resistivity does not drop to 0 completely, so we hesitate to classify this as a "superconducting film". Analysis of the binding energies in the film using x-ray photoelectron spectroscopy showed a severe tellurium deficiency in the film, resulting in

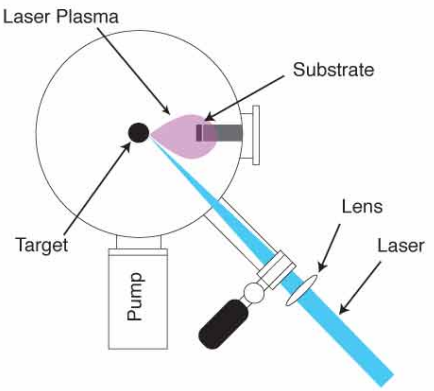

Figure 3.1: Schematic representation of a pulsed laser deposition process

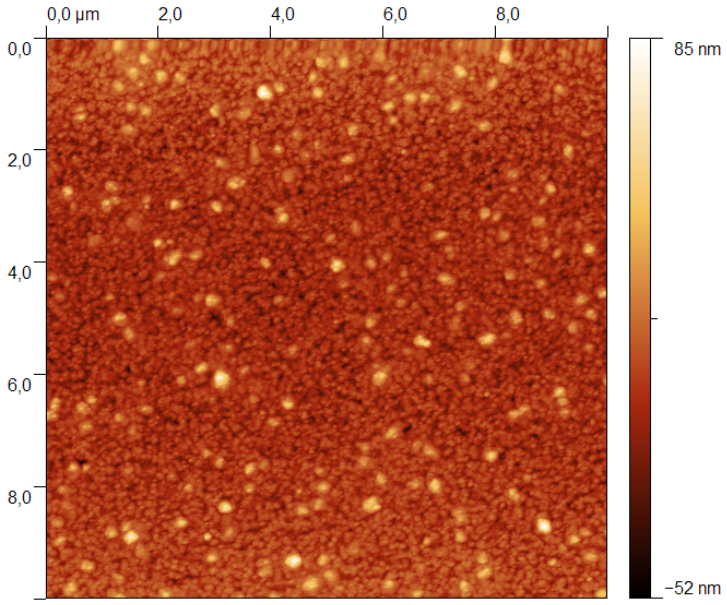

Figure 3.2: AFM image of a cold-grown (300K) film of $FeSe_{1-x}Te_x$ on LSAT after annealing, indicating very rough, island-like growth

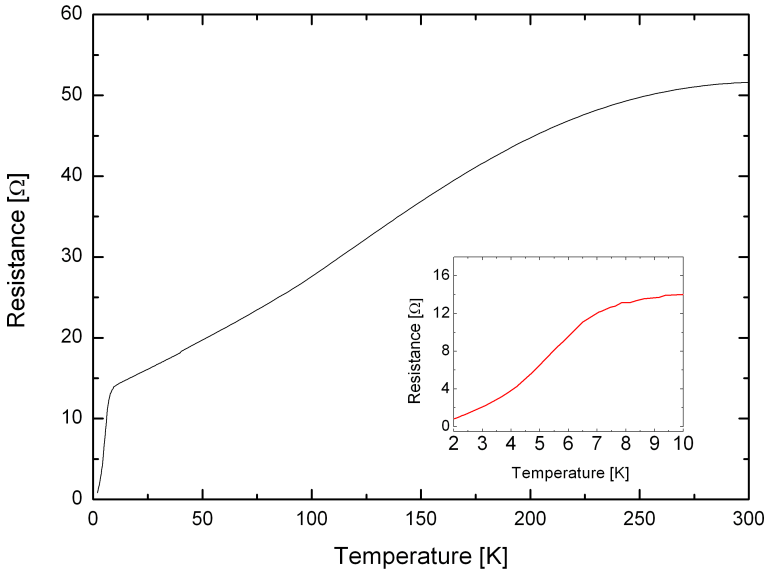

Figure 3.3: Almost-superconducting transition of an FeSeTe film on MgO, measured in a Van der Pauw configuration.

a lower T_c. We were unable to reproduce this result using the exact same deposition parameters, as all our attempts resulted in very rough insulating films.

Efforts continued to grow films in the proper configuration, but proved unsuccessful. Most films grown did not exhibit any electrical conductivity at all, with resistivities exceeding $\rho = 5 \times 10^4 \Omega$ m, which is the highest value we can measure in our current setup. The expected resistivity of a good quality thin film of iron selenide telluride would be orders of magnitude lower, as it is a so-called *bad metal* in the normal state ($T > T_c$).

However, some films did prove to be electrically conductive and showed an interesting temperature behavior. This is shown in Figure 3.4. We see an almost linear temperature dependence in a large temperature range, and on cooling down further, an exponential upturn of the resistance. This kind of behavior looks like that one would expect for a semiconducting material, but the linearity is striking and unexpected. It could be that this temperature dependence is the result of different phases present in the film, some insulating, some (semi-)conducting, et cetera. This film was grown at 10Hz, at 450° at a background pressure of 10^{-7}mbar with a target-substrate distance of 50mm.

After lowering the minimum attainable pressure in the chamber by replacing the roughing pump that creates the necessary low background pressure for the turbo pump to operate optimally, another film was grown. Films grown before this replacement were realized in a background pressure of 10^{-6} mbar or even higher, which increases the possi-

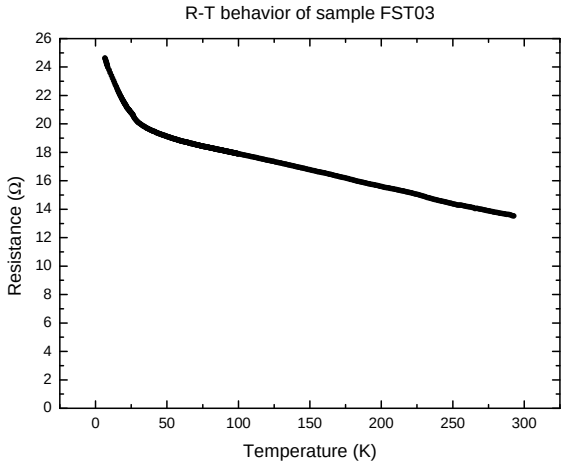

Figure 3.4: Resistance as function of temperature for sample FST03, 200nm on LSAT, measured in a four-point configuration

bility of sample contamination and alters the plasma emanating from the target. Usually, an inert gas like argon is used to shape the plasma plume, but as the plume size created by ablating iron selenide telluride is already quite small, all films reported in literature are grown in (ultra) high vacuum conditions, with $P < 10^{-6} mbar$. This new film was grown at a lower fluency of 2.5J/cm^2 at 450°, at a deposition frequency of 2Hz. These parameters were chosen after concluding that the best reported films were grown at the lower end of the indicated temperature range, for relatively low fluencies and deposition frequencies. Target-substrate distance was decreased from 50mm to 35mm, which however had the unintended consequence that the shutter could no longer be placed in front of the heater. This is done during pre-ablation, which removes any accumulated dirt and water from the target material. However, the result was unexpected, but appreciated.

After analysis in the Bruker diffractometer, the resistivity was studied in the RT setup (Fig 3.5). The film shows a clear superconducting transition with a $T_{c,onset}$ of about 9K and a $T_{c,0}$ of 5.4K. The anomalous behavior of the resistance at higher temperatures possibly indicates the presence of a semiconducting phase in addition to the (metallic) FeSeTe-phase. This could (partially) explain the lower critical temperature, which is expected to be around 14K for this compound. Another reason for the apparently lower critical temperature could lie in the presence of interstitial iron atoms, which partially suppresses superconductivity, resulting in a lower T_c. This effect was reported by McQueen *et al.*[35], who measured the disappearance of superconductivity in single crystalline samples of iron selenide, the parent compound of our iron selenide telluride, for samples with higher iron content. As we will see in a later section, we indeed conclude from susceptibility measurements that there is excess iron present in the thin film, and this is a viable explanation for the lower critical temperature.

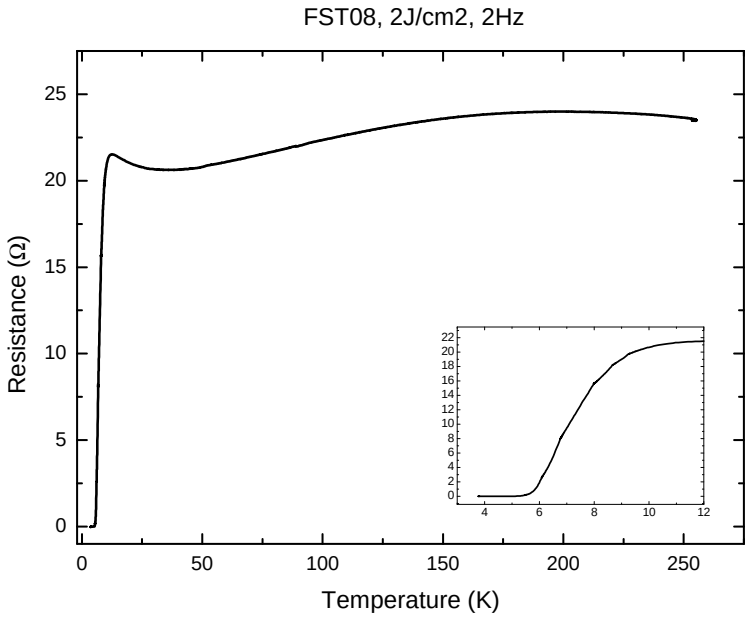

Figure 3.5: Resistance as function of temperature for sample FST08, measured in a Van der Pauw configuration

3.4 X-ray analysis of FeSeTe thin films

To gain insight into the crystal structure of the grown films, samples were characterized using both X-ray diffraction and – reflectivity scans. The former gives information about the crystallinity, lattice parameters and strain influence of the films, whereas the latter can be used to determine film thickness and – roughness. Both techniques are crucial in understanding the growth parameters of the material. Due to the significant surface roughness and thickness of the films, no meaningful data was extracted from the reflectivity scans, and they will not be further discussed.

3.4.1 X-ray crystallography basics

The principle of x-ray diffraction is based on the scattering of x-rays by a periodic structure, a crystal. This diffraction pattern depends both on the wavelength of the incident wave and on the periodicity of the sample under investigation. Because the typical interatomic distance in solids is of the order of Ångstroms, an incident wave should have a wavelength in the same order or smaller, and we end up using x-rays. The source of our diffractometer is a copper target material, yielding (mostly) Cu-Kα_1 radiation with a wavelength of 1.5405Å.

Due to the periodicity of the crystal, both constructive and destructive interference occurs for different angles. This interference pattern can, in a naive model, be understood using *Bragg's law*,

$$2d \sin\theta = n\lambda, \tag{3.1}$$

where d is the spacing between the crystal planes parallel to the surface and θ the angle of incidence of the x-ray wave. It is interesting to note that this condition only depends on the wavelength of the incident wave and the distance between the crystal planes, and not on the composition of these planes. A schematic overview of the Bragg condition is shown in Figure 3.6.

From a crystallographic point of view it's important to note that our substrate, LSAT, has a cubic structure (Fig. 3.7a, $a = b = c$), and FeSeTe exhibits tetragonal symmetry, where $a = b \neq c$ (Fig. 3.7b). The substrates are (001) oriented.

3.4.2 Experimental setup

All measurements were carried out in a Bruker D8 Discover diffractometer equipped with a Göbel mirror and a 2-bounce monochromator, which delivers a highly collimated beam of mostly Cu-Kα_1 radiation, with a minor component (about 4%) of Cu-Kα_2 radiation. To improve resolution, slits can be used to decrease scattering. Narrow (0.2mm) slits are used for aligning and reflectivity measurements for optimum resolution, and $\theta - 2\theta$ scans

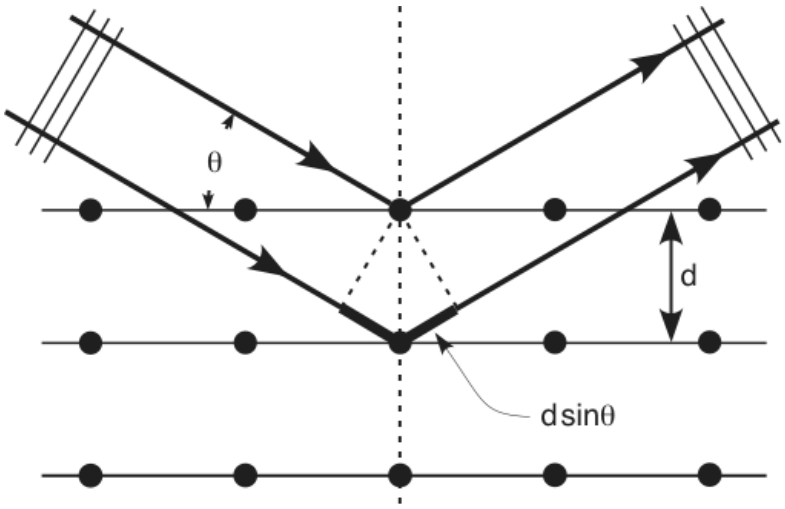

Figure 3.6: Schematic overview of Bragg diffraction

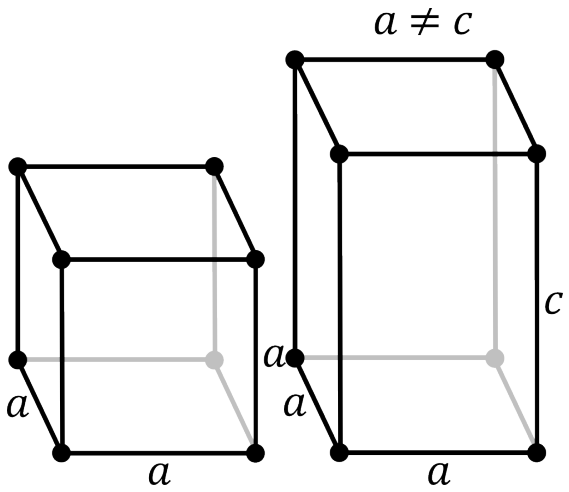

(a) Cubic crystal structure **(b)** Tetragonal crystal structure

Figure 3.7: Cubic and tetragonal crystal structures

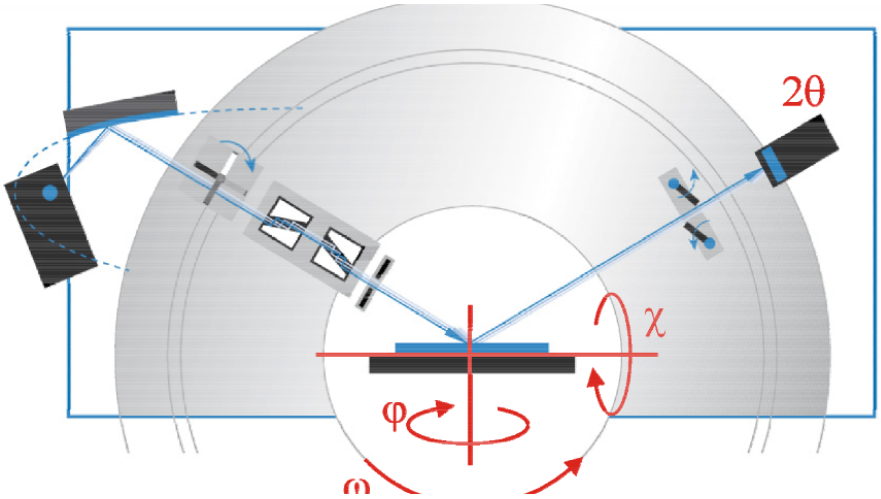

Figure 3.8: Schematic overview of the Bruker D8 diffractometer. From left to right: the X-ray source, Göbel mirror, rotary absorber, monochromator,slit, Eulerian cradle, slits, detector.

are carried out with larger slits of 1 and 2mm, which offered the best tradeoff between high resolution and beam intensity. A schematic overview of the diffractometer with all available axes is shown in Figure 3.8.

3.4.3 Lattice parameters of FeSeTe

The crystal structure of FeSeTe thin films on LSAT was studied using $\theta - 2\theta$ scans to establish the possible different phases present in the film, and to measure the tellurium content of the thin film, which is directly linked to the c-axis lattice parameter. This symmetric scan measures only crystal planes parallel to the surface, so it enables us to extract the lattice constant in the c direction, provided the film is epitaxially grown on the substrate. This is a default method to study epitaxial growth on substrates. From the position of the different (00l) peaks the lattice parameter c can be determined by solving the Bragg equation (3.1).

In order to evaluate the quality of the films, $\theta - 2\theta$ scans are compared with the provided target material which was used to ablate from. Figure 3.9 shows a $\theta - 2\theta$ scan of the target material, clearly showing the (00l) peaks of our target crystal. On zooming in on the individual diffraction peaks, a slight bump to the right of the main peak is visible, indicating a small different phase present. As noted in the article by Hsu *et al.*[32], varying the tellurium content results in different c-axis lattice parameters, the asymmetry in the (00l) peaks indicates a small spread in tellurium content of the target crystal. In principle, peak broadening is nothing abnormal, as it is caused by the finite thickness of the thin film, but asymmetry in the film peaks indicates the presence of inhomogeneities.

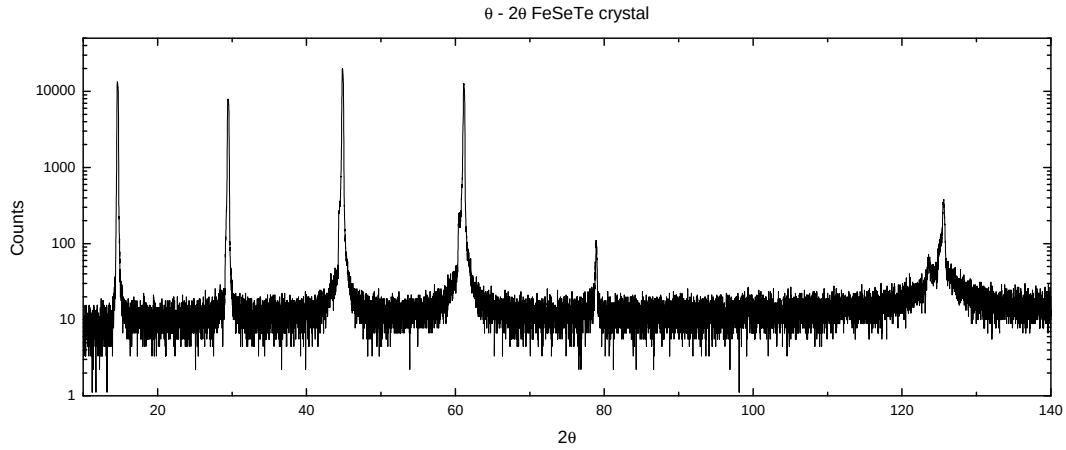

Figure 3.9: $\theta - 2\theta$ scan of the target crystal of FeSeTe

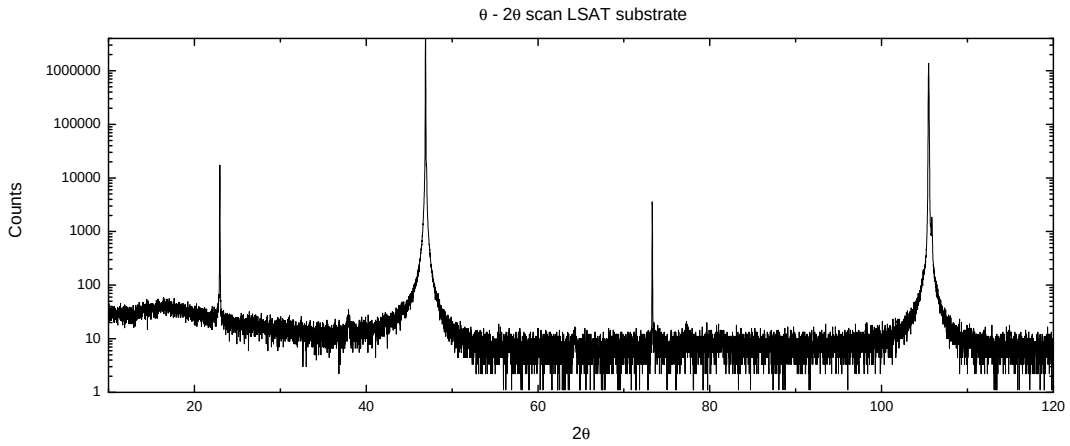

Figure 3.10: $\theta - 2\theta$ scan of an LSAT substrate

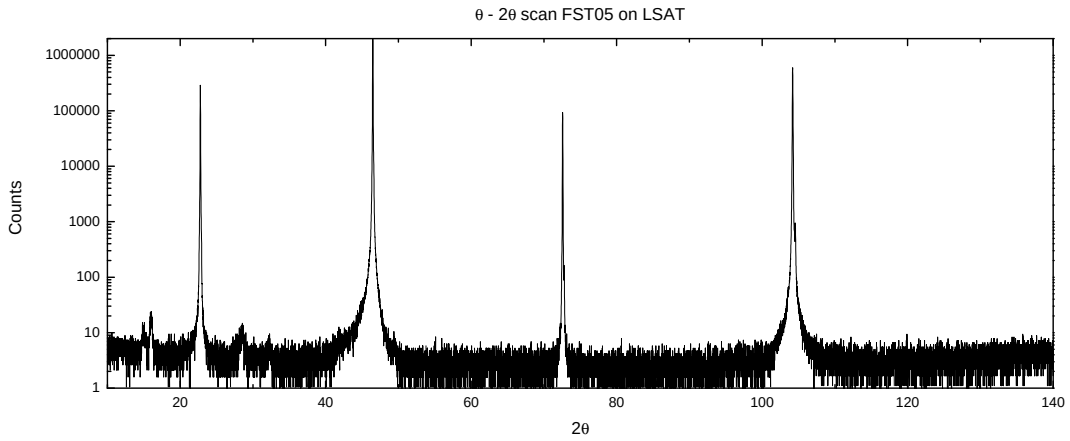

Figure 3.11: $\theta - 2\theta$ scan of the insulating film FST05 on LSAT

In Figure 3.10 the diffraction pattern from a similar $\theta - 2\theta$ scan on an LSAT substrate is shown, which can be used to compare with the film scan, in which these substrate peaks are clearly visible as well. The (001) orientation of the substrate is clearly visible from the position of the substrate peaks, and corresponds well to the values expected from literature.

Figure 3.11 shows a $\theta - 2\theta$ scan of sample FST05, which was grown at room temperature and subsequently annealed at 500 degrees Celsius. One can observe weak (00l) peaks belonging to the proper FeSeTe phase, in addition to another phase at lower angles. This indicates another phase is present in the compound, and could explain the poor electrical properties of the film. From this we conclude that growing a film at room temperature and recrystallizing it using vacuum anneal does result in partial epitaxial growth, but film quality is abysmal and a significant impurity phase is present, which proved detrimental for the electronic properties of the film. However, the stoichiometry which was determined by the *c*-axis lattice parameter does correspond well to the tellurium content in the target crystal.

The superconducting film, FST08, was analyzed as well. Figure 3.12 shows a high quality, *c*-axis oriented film with very little impurity phases present, except for a small presence of silver at 38°. This occurance of silver in the film is a well known phenomenon and can be attributed to the silver paint used to glue the sample to the heater during the PLD process. As with the previous sample, FST05, this film also shows broad, asymmetric peaks, indicating significant inhomogeneity in the composition of the film. However, the position of the maximum of the peak corresponds to a phase with a high tellurium content, which means this forms the majority phase in the film.

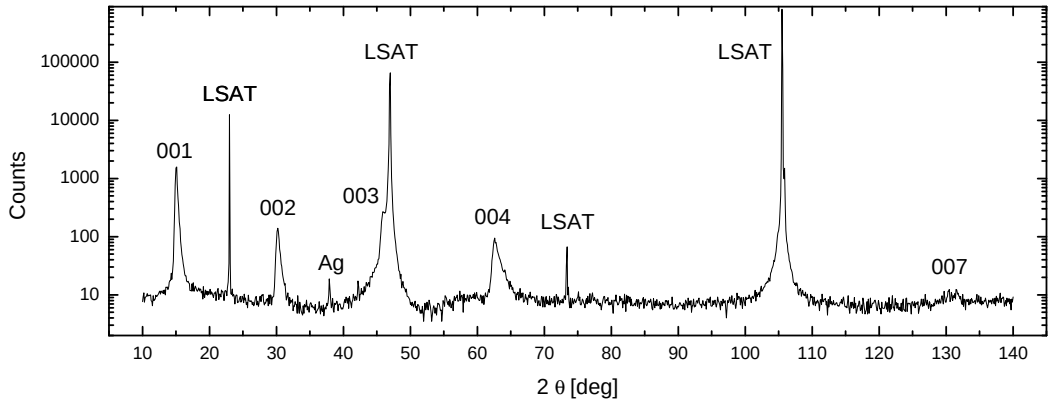

Figure 3.12: $\theta - 2\theta$ scan of the superconducting film FST08 on LSAT

To extract the lattice parameters of the films, we need to analyze the different peak positions and solve the Bragg equation for each of them, which yields the c-axis lattice parameter for the symmetric $\theta - 2\theta$ scan. Some previous work[34] assumes a constant unit cell volume and thus calculates the a-axis lattice parameter from the measured c-axis lattice parameter, however here this is not the case, as unit cell volume is not conserved when the c-axis enlargement is caused by selenium substitution by tellurium. It does hold when strain causes the unit cell to stretch in order to match the substrate, but this is not the case here.

Of course, the values we measure for the different crystallographic directions are prone to certain errors, both systematic and random. These errors have been widely studied and found to be minimal for $\theta = 90°$, so by measuring different peaks for the same material (the $00l$-peaks, for example) and calculating a linear regression through these points, when plotted versus what is known as a *Nelson-Riley function (NR)*, the most accurate value for d is extrapolated for $\theta = 90$ or $NR = 0$[36]. The Nelson-Riley function is given by

$$NR = \frac{\cos^2\theta}{\sin\theta} + \frac{\cos^2\theta}{\theta} \tag{3.2}$$

As can be seen from Figure 3.13, for the five peaks present in our film, the fit is rather abysmal, but with significant error in the exact position of the peaks, this is to be expected. However, this only slightly varies the value of the extrapolated lattice spacing, and differs very little from the usual approach of determining the lattice parameter by doing a least-squares fit of the lattice constant versus θ.

A good way to determine the lattice parameters of the film would be to make a reciprocal

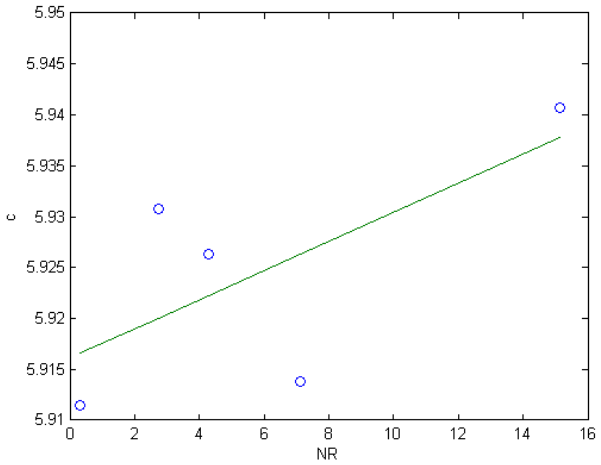

Figure 3.13: Lattice parameter fit using the Nelson-Riley functions. The best fit for the lattice parameter is found for NR=0, however significant deviation from the ideal fit are clearly visible

space map of the sample, which shows the (hkl) parameters of both film and substrate in a single two-dimensional plot. However, this requires significantly strong out-of-plane peaks for both the substrate and film to lie within a few degrees (in 2θ) of each other, as well as on a similar plane in χ. We did not find a suitable pair of diffraction peaks for FeSeTe on LSAT, and thus had to look for a different way to measure the out-of-plane lattice parameter for our c-axis oriented film.

The solution lies in the fact that with a symmetric scan, one measures only the planes perpendicular to the vector that bisects the incoming and reflected beam. By tilting the sample under a certain angle χ, we measure the (101) planes of the film (Figure 3.14). Then, by once more applying Bragg's law, we can extract the a-axis lattice parameter, for a given (measured) value of c. The (101) $\theta - 2\theta$ scan is shown in Figure 3.14. Clearly visible are the (101), (202) and (303) peaks, where the latter coincides with the (640) diffraction peak of the LSAT substrate. χ was tilted at 57.2°.

From these scans, we conclude that the c-axis lattice parameter of film FST08 is equal to 5.92Å, and a is equal to 3.82Å. This corresponds well to values found in literature[33, 31, 16].

3.4.4 Stoichiometry

There exists an interesting link between the crystal structure of the iron-based superconductors and their superconducting properties. For example, Hsu et al. showed [32] a direct link between the critical temperature T_c and anion height in these compounds, which means, the height of the anion (Se, Te, etc.) above the Fe-plane determines the

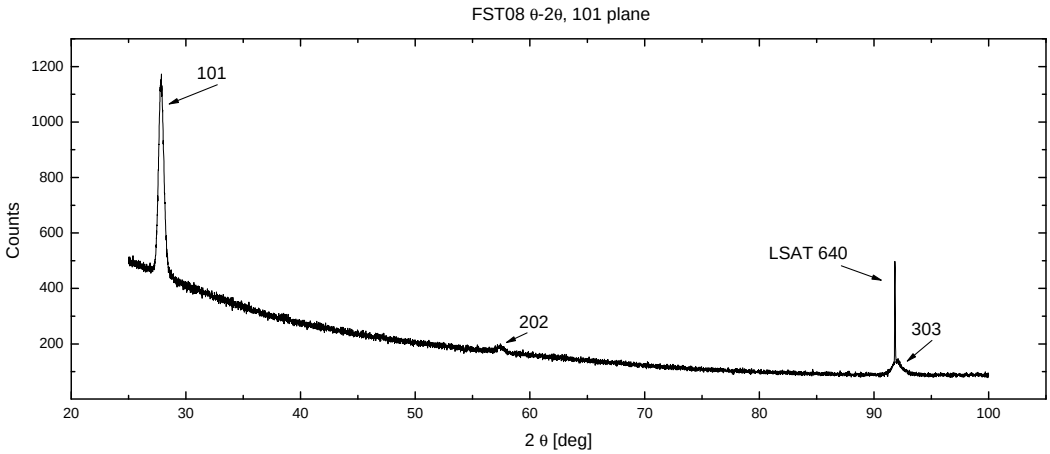

Figure 3.14: $\theta - 2\theta$ scan of the (101) planes of sample FST08

angle between the iron atoms and the other ions in the compound, and T_c is maximized when this angle approaches that of a perfect tetrahedron.

In a similar way, it seems like a similar mechanism is responsible for the increase in T_c in iron selenide telluride, where the critical temperature increases when increasing the tellurium content from zero to a maximum at around a Te content of 50%. Now because tellurium has a bigger atomic radius than selenium does, the average anion height for a Te-rich compound will be higher than the average anion height in a Te-deficient compound. This, in turn, determines the c-axis lattice parameter of the crystal, as these compounds exhibit a tetragonal crystal symmetry.

This way, we can say something about the tellurium content of a thin film or crystal by examining the crystal's c-axis lattice parameter, which is easily measured in a $2\theta - \omega$ diffraction pattern. This was shown by Wu et al, [37], who determined the c-axis lattice parameter for different compositions of $FeSe_{1-x}Te_x$. Figure 3.15 shows the change in (00l)-peak position in for varying tellurium content.

In the first superconducting thin film, 3.3, we explained the lower critical temperature of 8K by the fact that it's c-axis lattice parameter was measured to be significantly smaller than the target crystal's lattice parameter, indicating a lower tellurium content. However, in the last film grown, the tellurium content was measured to be approximately 50%, which corresponds to an optimally doped film. However, the critical temperature was still only 9K, but with a better, steeper superconducting transition. One hypothesis is that defects in the film, vacancies, grain boundaries and the like, significantly lower the critical current of the film, leading to a lower critical temperature. However, this means that still the grains in the film could have higher T_cs. To investigate this, it's

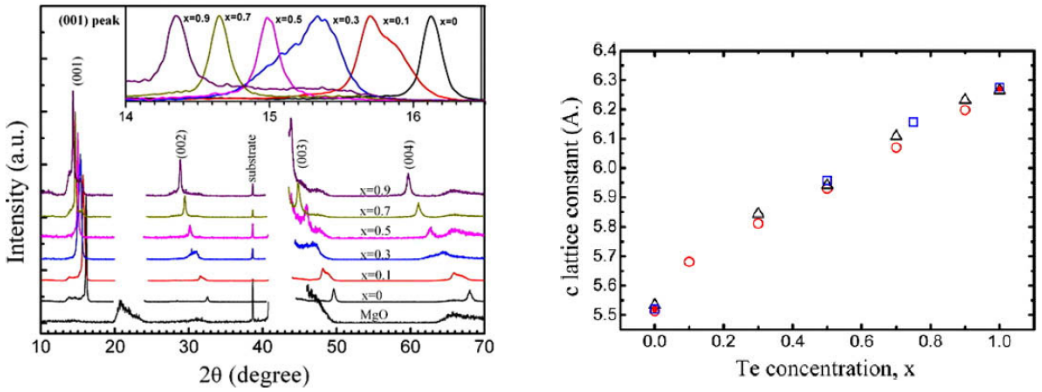

(a) (00l) peaks of $FeSe_{1-x}Te_x$ thin films for varying tellurium content

(b) Tellurium content as function of the c-axis lattice parameter

Figure 3.15: Increasing c-axis lattice parameter for higher tellurium concentrations in thin films of $FeSe_{1-x}Te_x$ as described by Wu *et al*[37]

worthwhile to look at the temperature dependence of the magnetic susceptibility of the compound.

One of the basic properties of a superconductor is that as it reaches the critical temperature, the magnetic susceptibility χ drops to a negative value, because of the Meissner effect, which is a diamagnetic effect. By measuring the susceptibility as function of temperature, we can determine the critical temperature at which this phase transition takes place. As this measurement is carried out without the need for a transport current, any grain boundary effects are not taken into account, and it allows us to determine the critical temperature of the individual grains.

However, a complication of this approach in the case of $FeSe_{1-x}Te_x$ is the likely presence of (paramagnetic) iron impurities in the film. Iron, which has a strong magnetic moment, exhibits a strong positive susceptibility, and it's very well possible that the signal from the iron "impurities" masks any diamagnetic response from the superconducting volume fraction in the film. However, if we can account for these different contributions, we can hopefully see a clear dip in the magnetic susceptibility at T_c, and thus determine the superconducting volume fraction of the film.

3.5 Magnetic measurements

As noted in the previous sections, the critical temperature as measured in the R-T setup does not correspond to the expected T_c for the optimally doped FeSeTe-compound. Investigation using XRD as described in the last paragraph indicates the stoichiometry of the grown film corresponds well to the stoichiometry of the used target, which should result in a T_c of about 14K. This means that the lower T_c has to be caused by some other

(macroscopic) phenomenon that quenches superconductivity at higher temperatures. One hypothesis is that the individual grains themselves do become superconducting at high temperatures, but if a significant fraction of the film has the wrong stoichiometry with a lower (if at all) T_c, this could result in a percolation path only becoming closed at the critical temperature of the weakest grains that are necessary to create a fully-connected percolation path. This is something that's an inherent complication when testing for superconductivity using a bias current: one needs to be able to actually drive a current through the film.

An alternative way of establishing the critical temperature of a film is to look at the magnetic properties of the film. The base compound of iron selenide telluride is a bad metal at temperatures $T > T_c$, showing interesting magnetic properties like antiferromagnetic ordering, spin density waves and other related phenomena. However, upon transition through the critical temperature, the compound becomes strongly diamagnetic, an effect known as the Meissner-Ochsenfeld effect. This means that the superconductor will actively expel magnetic flux from its interior by creating circulating supercurrents at the surface of the material that screen out the magnetic field.

This should be visible when measuring the magnetization of the film as a function of temperature. The magnetic moment of the superconductor should change from a (small) positive value above T_c to a significant negative value for temperatures below the critical temperature. We performed such measurements in a vibrating sample magnetometer (VSM) inside a Quantum Design physical properties measurement system or PPMS. In this experiment, the sample is quickly moved up and down in a set background field, and the magnetization response from the sample is measured by a pickup coil which is located around the sample. This results in a magnetization curve, which is shown in Figure 3.16. Note that the sample has been cooled down in zero field, after which a field of 1000Oe is applied and the temperature sweeped from 4K to 200K.

As we can see from this figure, the sample unfortunately does not show any indication of a superconducting transition. (Figure 3.17). An interesting feature is the sudden jump in magnetic moment at 65K, which corresponds to a phase transition in the FeSeTe compound which has been seen in other work[38].Converting the measured magnetic moment in Am^2 to a magnetic moment per unit cell, the film shows a magnetic moment of approximately $0.08\mu_b$, where μ_b is the Bohr magneton, the natural unit for magnetization. One Bohr magneton corresponds to the magnetization caused by a single unbound spin per unit cell. In this case, it indicates that for every twelve unit cells, one individual spin is present which contributes to the total (paramagnetic) magnetization of the sample. Also, for low temperatures the film shows paramagnetic behaviour, where the magnetization increases with decreasing temperature, indicative of paramagnetism. This could well be caused by interstitial iron atoms present in the sample. To see if any ferromagnetic phases are present in the compound, it would be worthwhile to measure magnetization curves as function of the applied field (M-H curves) to see if any hysteric effects can be measured, which are a clear sign of ferromagnetism. Another reason for the lack of clear diamagnetic response in the magnetization could be that the sample

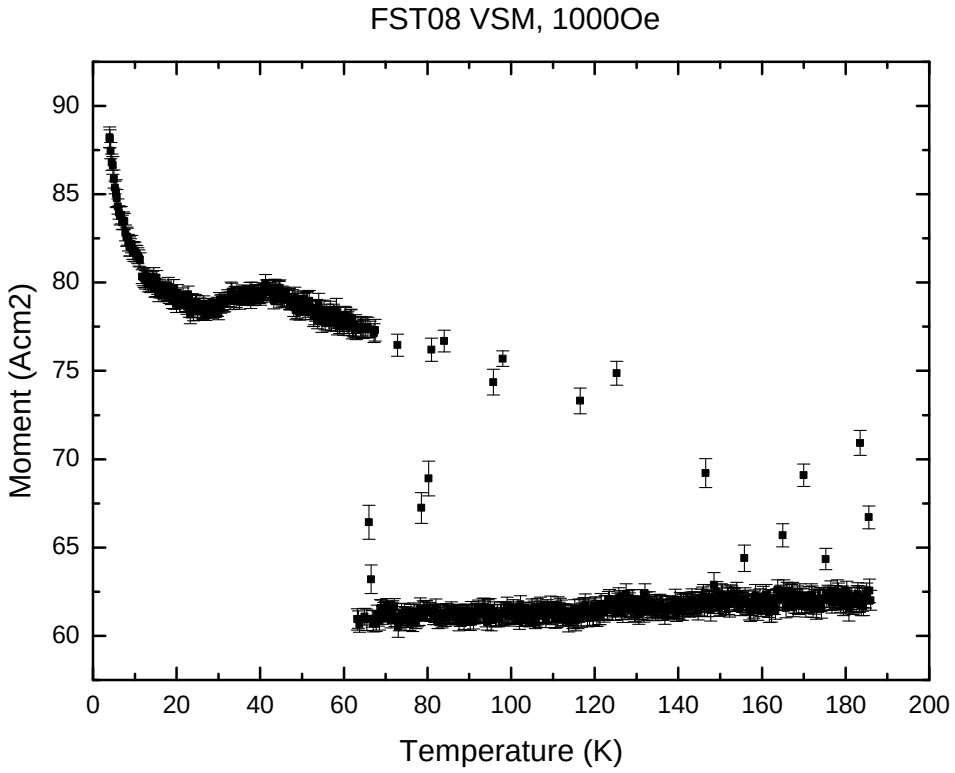

Figure 3.16: Magnetic moment versus temperature for the superconducting sample FST08

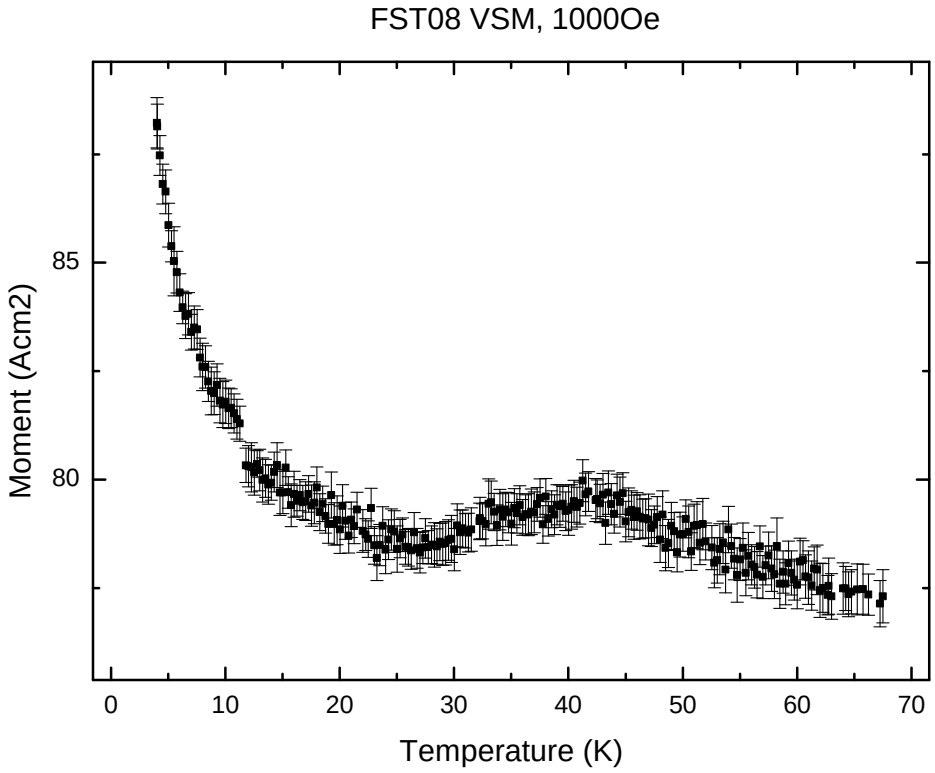

Figure 3.17: Magnetic moment versus temperature for the superconducting sample FST08

was cooled in a small background field, resulting in trapped vortices in the film. There is a known difference reported in literature between magnetization curves for zero field and nonzero field cooling measurements. However, this is relatively unlikely, as the background field in the PPMS is of the order of Gauss, and the critical fields of FeSeTe are in the order of tens of thousands of Gauss.

3.5.1 Investigation of defects

Defects can have great influence on the superconducting properties of films. For example, grain boundaries and twinning decrease the critical current between grains, which is detrimental to a good performance of the film and devices made on it. This is usually not a problem in (metallic) BCS superconductors, with coherence lengths in the order of hundreds of nanometers, but as with the cuprates, the iron pnictide and chalcogenide superconductors exhibit very short coherence lengths, meaning grain boundaries possibly become a significant problem for superconducting transport. Control and proper analysis of defect densities is thus of utmost importance, and should be studied. The relatively broad superconducting transition we observed in films, and the non-superconducting films lead us to investigate the defects in our films.

A great tool to investigate crystal defects is a so-called rocking curve, where we slowly vary θ around a film peak whilst keeping 2θ constant. The width of this peak then tells us something about the defect density and disorder in the film. A high-quality film with a low defect density will show a very sharp peak, whilst a disordered film will be indicated by a broad peak in the rocking curve.

Figure 3.18 shows such a rocking curve for film FST08, which is superconducting.Also, we can compare this rocking curve to one from the target crystal, which is shown in Figure 3.19.

Looking at the full-width half-maximum (FWHM) of the rocking curve, we notice immediately that the curve for the thin films is much broader than the one from the crystal. This shows the crystal is of higher crystalline quality (less defects), although it seems like two different orientations are present in the target crystal, as can be seen from the two individual maxima in the rocking curve. This should however not influence the quality of the thin film, as only stoichiometry is really important, since crystallinity is only realized upon nucleation of the film.

Another check for the epitaxy of the grown film is to look at the orientation of the film compared to that of the substrate. A good check for this is to examine a peak with both in- and out-of-plane miller indices, and perform a ϕ scan, which should show fourfold symmetry for the LSAT substrate. If we see the exact same (101) peak positions for both the LSAT and FeSeTe thin film, we can conclude the film has grown in the same orientation as the substrate has. Such a ϕ-scan is shown in Figure 3.20. It's clear from this graph that the maxima of the (101) peaks for both the LSAT and FeSeTe coincide, leading to the conclusion that indeed the film is grown epitaxially on top of the substrate,

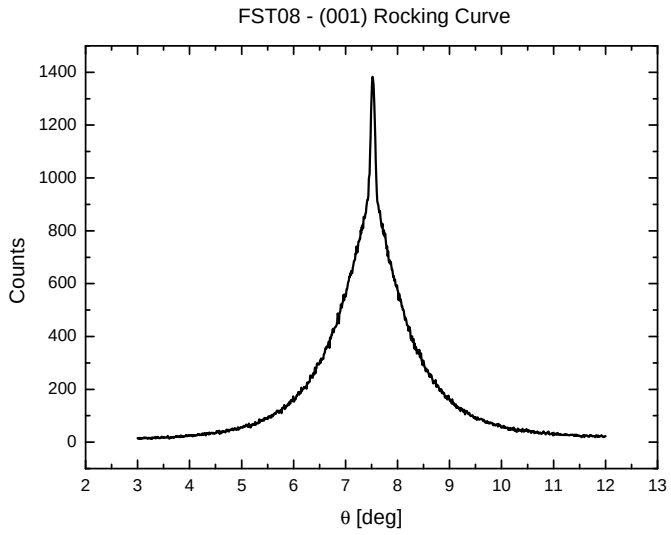

Figure 3.18: Rocking curve around the (001) peak of sample FST08

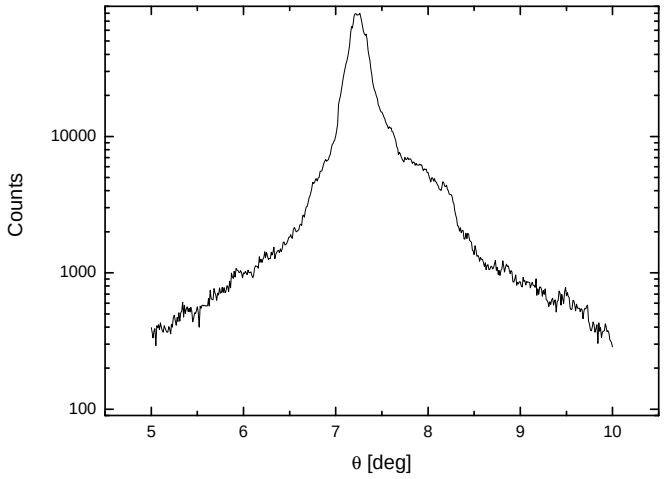

Figure 3.19: Rocking curve around the (001) peak of the FeSeTe crystal

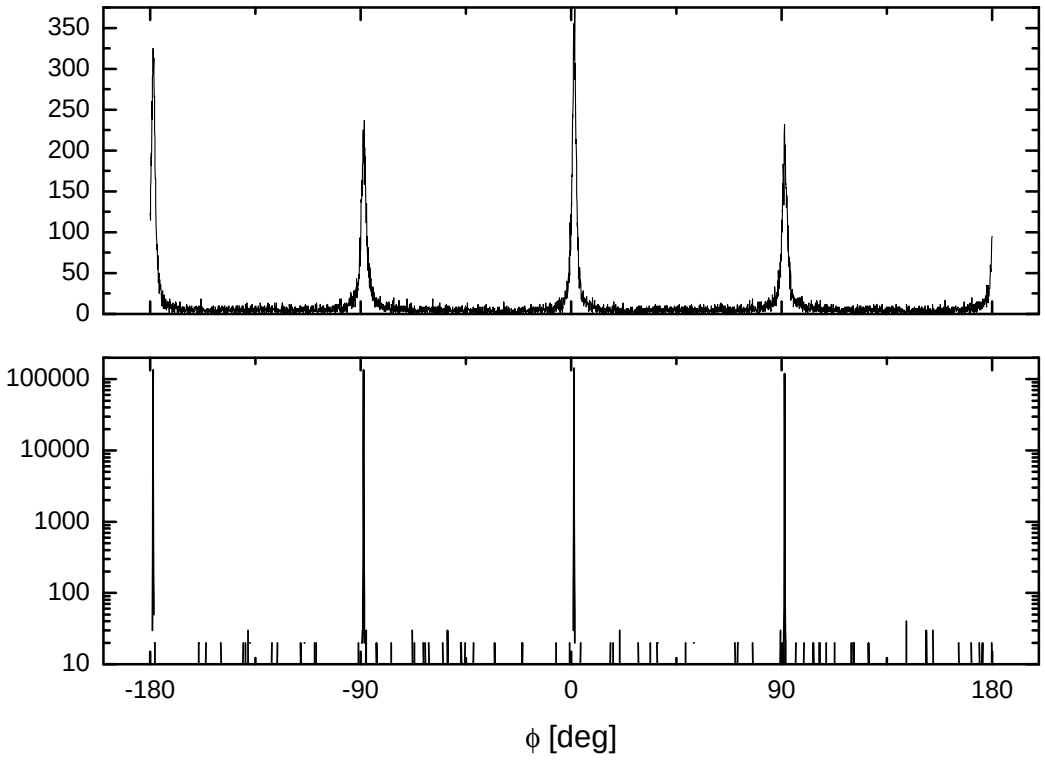

Figure 3.20: ϕ-scans for the LSAT substrate and epitaxially grown FeSeTe thin film

without any hexagonal or other phases present. In addition to this, the 90° separation of the peaks clearly indicates fourfold symmetry, corresponding to the tetragonal phase of the superconductor.

3.6 Concluding remarks

During this project, it quickly became obvious that growing thin films of iron selenide telluride is no simple feat. However, after much trial and error we managed to produce a superconducting film which has a clear superconducting transition with a $T_{c,onset}$ of 11K and a $T_{c,0}$ of 5.5K, where the large ΔT_c can most likely be attributed to defects in the crystal and inhomogeneities in the film, which are obvious from the broad peaks in the $\theta - 2\theta$ peaks and rocking curves in x-ray diffraction experiments. Also, the rough surface morphology with multiple "dots" and pinholes indicate island-like film growth,

where superconductivity is only measured for increasingly thick films, which could well indicate percolation-type conductivity. Also, the lower critical temperature we measured in transport indicates grain boundaries play a significant role in the properties of the film, and stoichiometry of the individual grains does not tell the whole story here. J_c measurements on these films would be very interesting to further investigate these effects.

Finally, when summarizing our results with those available from literature it seems like the best superconducting films are grown at relatively low temperatures, at relatively low deposition frequencies and -energies, with the substrate placed relatively close to the target. Only when we moved the sample significantly closer to the target, we obtained proper results. A significant disadvantage of the current PLD system is the minimum heater-target distance of 45 millimeter, which, when assessing the size of the plume emanating from the target on laser impact, is too big a distance, and could well explain the significant amount of particulates present on the surface.

4 Conclusions and Recommendations

4.1 Junctions on $FeSe_{0.4}Te_{0.6}$

Using conventional photolithography, NS- and S-I-S junctions were fabricated on single-crystalline flakes of $FeSe_{0.4}Te_{0.6}$. The aluminum - FeSeTe NS junctions show conductance spectra similar to those obtained for a junction with interface height Z of approximately 0.5, and a mixing parameter α of 0.2. For a clear indication on the order parameter symmetry of FeSeTe, one would ideally grow a tunnelbarrier, that is, a junction with a Z value much larger than 1. The $s^{\pm}$ symmetry of the superconducting order parameter would be shown by the presence of Andreev bound states at finite voltage, due to the interference of the two tunnel modes in the junction.

The niobium - FeSeTe junctions showed clear Josephson characteristics, with a junction area of approximately $2\mu m^2$, assuming only c-axis junctions contributing to the supercurrent. However, the significant thickness of the flake means that ab-axis contact can not be neglected, even though the application of a magnetic field perpendicular to the ab-plane did not show any significant critical current modulation. The junction shows an I_c of $5\mu A$, which, combined with the normal state resistance of the junction gives an I_cR_n value in the order of microvolts. This indicates a low-quality junction, as for a good Josephson junction this product should be of the order of the superconducting gap, which is in the order of millivolts. This low I_cR_n product could well be caused by the low quality of the insulating barrier, which is formed by residual oxides and water present on the interface of the FeSeTe flake before deposition the niobium leads. Because the barrier is not controlled well, it could possibly have pinholes or other inhomogeneities in it, which leads to lower junction quality. The growth of a well defined, uniform interface barrier, as with the NS-junction, should improve the junction characteristics. This could be done *in situ* in the Nordiko sputter system by growing a thin (10Å) layer of aluminum on the flake, which is then left to oxidize in the Nordiko's load lock for 30 seconds. This aluminum oxide now forms the insulating barrier between the FeSeTe flake and the niobium lead.

An attempt at creating a S-I-S junction on a very thin flake of FeSeTe failed, as the junction behaved like a normal metal - superconductor junction, showing a peak in the conductance at the gap value of niobium. This could either be caused by the decrease of ab-axis tunneling or the fact that thin flakes of FeSeTe simply do not become superconducting. More experiments need to be done on this to clarify this matter. For example, a good first step would be to cover the sides of the flake with an insulating barrier, after

which a pure *c*-axis contact can be grown by sputter deposition of the material of choice. This should eliminate any *ab*-axis contribution to the total conductance.

An overall conclusion with regard to the junctions made on thin flakes of FeSeTe is that in order to obtain high-quality junctions, interface quality and control is of utmost importance, to make sure that "features" in the measurements are not caused by imperfections in the junctions, but are really a consequence of the underlying physics of the materials. This is quite feasible, as growing a high-quality aluminum oxide barrier of variable thickness can be grown in the same production step as the aluminum or niobium contacts.

Furthermore, when good quality, homogeneous thin films of FeSeTe are available, ramp-type junctions should be made to test the difference in transport properties of in- and out-of-plane junctions. Due to the threedimensional, anisotropic shape of the order parameter in these materials, this could be an interesting way to see if a phase-sensitive experiment can be designed by combining an in-plane and out-of-plane oriented junction in a single circuit.

4.2 $FeSe_{1-x}Te_x$ thin films

A superconducting film of $FeSe_{1-x}Te_x$ was grown using pulsed laser deposition at a temperature of 450°C. The laser fluency used was 2.5J/cm^2 on a spot of 2×2mm^2. The film showed a clear $T_{c,onset}$ of 9K and a $T_{c,0}$ of 5.3K. However, after magnetization measurements we conclude that only a small superconducting volume fraction exists in the thin film, as no diamagnetic response was observed at the expected critical temperature of 14K. The discrepancy between the critical temperature of the film and the expected values which have been reported in literature we were unable to account for, and was investigated using X-ray diffraction. The bad superconducting properties of the film, and other films grown, can possibly be attributed to the large (4.5cm minimum) substrate-target distance. This is a limitation of the PLD chamber used to grow the films, and this problem cannot be solved in the current configuration. The shorter-than-usual required substrate-target distance is caused by the very small plasma plume emanating from the target upon laser irradiation. It is known that the optimal position of the substrate is at the edge of the plasma plume, to ensure correct stoichiometric transfer of material from the target to the substrate.

The $\theta - 2\theta$ diffraction scans of the superconducting film showed clear *c*-axis oriented growth, with no parasitic phases present. A minor presence of silver was measured, which can be explained by the use of silver paste during film growth. The *c*-axis lattice parameter of the thin film was determined using this $\theta - 2\theta$ scan by means of the Nelson-Riley method, which accounts for possible errors in the measurement, and was determined to be 5.91Å. Using this result, the in-plane lattice parameter of the tetragonal FeSeTe was determined from a $\theta - 2\theta$ scan of the (101) planes of the material. This was done by rotating the χ-angle of the diffractometer by 57.2°, which fulfills the Bragg

condition for these planes. Using this approach, the a-axis lattice parameter was determined to be 3.81Å, which, compared to the lattice parameter of the LSAT substrate, indicates the film is fully relaxed on the substrate and strain is not present. However, due to the mismatch in crystal plane alignment, reciprocal space maps could not be made of the thin film and substrate. This would give clear insight in the possible presence of strain in the film.

The presence of tellurium in a thin film of $FeSe_{1-x}Te_x$ is directly related to the c-axis lattice parameter. Comparing the c-axis lattice parameter for the grown film to values from literature, we conclude the grown film has a composition of $FeSe_{0.5}Te_{0.5}$, which is the optimally doped stoichiometry for this material with an expected T_c of 17K.

Using rocking curves, the presence of defects in the grown film was studied. This is of significant importance, as the quality of a thin film in terms of electrical transport is directly related to the presence of defects. FWHM values for the (001) peak of both the target crystal and thin film were compared, and were found to be much higher in the thin film. As this FWHM value of the rocking curve is directly related to defect density we conclude that significantly more defects are present in the thin film, compared to the target crystal.

The alignment of the thin film on the substrate was studied by performing ϕ-scans of the (101) peaks of both the LSAT substrate and the FST thin film. Perfect fourfold symmetry was observed for both the substrate and the film, with the different (101) peaks lining up perfectly, indicating good alignment of the thin film and the substrate.

4.3 Possible improvements to the Edward PLD system

During this research projects, the limitations of the PLD system we coined *Edward*, after Murphy, were quickly discovered. The controller fails at random intervals, even though it is connected to an uninterruptable power supply (UPS). It seems to lose its settings regularly, and becomes unresponsive. Also, the presence of many controllable motors in the system quickly fills up the available memory for controller software. This means that vital functions like changing the target-substrate distance are not available on demand, and the growth process has to be stopped before this can be changed. Also, the shutter, which is opened by another stepper motor, does not operate well, as the motor can only just provide the torque needed to rotate the shutter axis. If this fails, the entire system crashes and all alignment needs to be redone, which is higly undesirable and has lead to many lost hours.

The target is aligned in the system with the alignment laser mounted on the KrF excimer laser used for deposition. Because the beam path to the system passes two UV-mirrors, which are quite transparent to visible light, the intensity of the alignment laser exponentially decreases for every added mirror. This means only a very faint spot is visible on the target, and because no viewport is available to look at the target other than the

one acting as laser window, it is very hard to align the target in the laser beam.

There are a number of changes that could be implemented to improve the reliability, userfriendliness and throughput of the system. First of all, all stepper motors on the system are unnecessary, except for the three stages controlling target movement. As the target is scanned in a rectangular pattern through the laser beam, and not rotated, as in most of our other systems, these three motors are of vital importance. They operate flawlessly, and do not need redesigning. However, the stepper motors that control the heater position are unnecessary, as this could easily be done by hand, which has the added benefit of being able to fine-tune the heater position to ensure the substrate is at the right position during deposition. The stepper motor controlling the shutter is unnecessary and even potentially endangers the functionality of the system. Before the shutter is lowered, the heater needs to be moved back so the shutter can lower in front of the heater. However, due to the instability of the controller which engages the motors in the system, the shutter has, on multiple occasions, crashed into the heater before the heater was fully out of the way. This damages the heater manipulator stick, and the system has to be de-assembled to execute the necessary repairs. Therefore, I advise to remove all stepper motors except for the ones controlling the target movement during deposition.

Doing this also frees up vital lines of memory in the controller, which can then be used to implement better checks in the software, to improve the reliability and user-friendliness of the system. The heater stage and shutter can, and should be, operated by hand to ensure optimal flexibility when operating the system. Also, to improve on the alignment issue, it would help a lot if the beamline for the laser could be reduced to a single mirror or even no mirror at all.

The system as it exists today is not equipped with a load lock. For an ultrahigh vacuum system, this significantly limits the maximum attainable throughput of the system, in terms of films per day. The only way we can currently attain pressures of 10^{-8} mbar is when the system is degassed at 100°C for at least 24, preferrably 48 hours. Equipping the system with a loadlock would significantly increase the usable time of the system, and minimize downtime.

5 Acknowledgments

Een Master-onderzoek doen is mooi, maar onmogelijk zonder de hulp van anderen. Ik heb met heel veel plezier gewerkt in de Interfaces and Correlated Electron systems groep, en heb het geluk gehad een beroep te kunnen doen op de grote hoeveelheid kennis en kunde die hier aanwezig is. Ten eerste ben ik dank verschuldigd aan Hans Hilgenkamp, die mij vanaf mijn Bacheloropdracht heeft betrokken bij de ICE (toen nog CMD) vakgroep. Hans, je brede kijk op de wetenschap en alles wat daar mee te maken heeft, alsmede je support in lastige tijden heb ik heel erg op prijs gesteld. Alexander Brinkman ben ik veel verschuldigd voor alle keren dat ik je kantoor ben binnengestormd met data, vragen of wat dan ook. Jouw deur staat écht altijd open. I am very happy to have had the opportunity to discuss the physics of iron-based superconductors with yet another Alexander. Sasha, thank you for your patience and clarity in explaining the hardest theoretical concepts in such a way that I could follow you and use it to improve on my knowledge. Sybolt, dankjewel voor je hulp bij de X-ray experimenten en voor alle mooie verhalen in de koffiekamer.

The advantage of not having a PhD student or postdoc as your direct supervisor is that there's more of them available if you need help with something. In non particular order, I owe a lot to Aleksandar, Francesco, Menno, Marieke, Cor, Denise, Hidde, Wiemer, Sander, Sander, Peter, Bernard and Joost. Thank you so much for sharing everything you know about the lab and the physics we're studying together. The coffee breaks and *fruithapjes* are something I will definitely try to keep attending from time to time. Een speciaal woord nog voor mijn voorganger op dit project, Diederik. De eerste hectische maand zal ik waarschijnlijk nooit meer vergeten, al heb ik mijn uiterste best gedaan om het aantal uren wat we toen maakten nog even te overtreffen in míjn laatste maanden. Dankjewel voor de grote hoeveelheid werk die je hebt verricht bij het opstarten van dit project.

Wetenschappers zijn een bijzonder soort mensen dat goed in het gareel moet worden gehouden. Deze groep zou niet draaien zonder de fantastische hulp van Frank, Dick, Ans, Inke en Harry. Dank jullie wel voor alles.

Dan mijn familie. Het heeft even geduurd, maar dankzij jullie onvoorwaardelijke steun ben ik dan nu toch echt klaar. Dank jullie wel voor jullie enthousiasme en pogingen om te begrijpen wat ik in hemelsnaam allemaal aan het doen was hier. Als laatste een verschrikkelijk groot woord van dank voor Janneke, mijn lief. Wat heb jij het zwaar gehad met mij. Ik heb verschrikkelijk veel zin in onze toekomst samen. Tijd om verder te gaan!

Bibliography

[1] H Kamerlingh Onnes. The superconductivity of mercury. *Communications from the Physical Laboratory of the University of Leiden*, 122, 1911.

[2] J. Bardeen, L. N. Cooper, and J. R. Schrieffer. Theory of Superconductivity. *Physical Review*, 108(5):1175–1204, December 1957.

[3] Leon Cooper. Bound Electron Pairs in a Degenerate Fermi Gas. *Physical Review*, 104(4):1189–1190, November 1956.

[4] National High Field Magnetic Laboratory. http://www.magnet.fsu.edu/education/tutorials/magnetaca

[5] J. G. Bednorz and K. A. Mller. Possible highT c superconductivity in the Ba?La?Cu?O system. *Zeitschrift fr Physik B Condensed Matter*, 64(2):189–193, June 1986.

[6] J. R. Kirtley, C. C. Tsuei, J. Z. Sun, C.C. Chi, Lock See Yu-Jahnes, A Gupta, M Rupp, and M. B. Ketchen. Symmetry of the order parameter in the high-Tc superconductor YBa2Cu3O7-delta. *Nature*, 373(19 january), 1995.

[7] Yoichi Kamihara, Hidenori Hiramatsu, Masahiro Hirano, Ryuto Kawamura, Hiroshi Yanagi, Toshio Kamiya, and Hideo Hosono. Iron-based layered superconductor: LaOFeP. *Journal of the American Chemical Society*, 128(31):10012–3, August 2006.

[8] Igor I Mazin. Superconductivity gets an iron boost. *Nature*, 464(7286):183–6, March 2010.

[9] Alexander Balatsky and David Parker. Not all iron superconductors are the same. *Physics*, 2, July 2009.

[10] DJ Van Harlingen. Phase-sensitive tests of the symmetry of the pairing state in the high-temperature superconductors. *Reviews of Modern Physics*, 1995.

[11] Hans Hilgenkamp. Pi-phase shift Josephson structures. *Superconductor Science and Technology*, 21(3):034011, March 2008.

[12] C.-T. Chen, C. C. Tsuei, M. B. Ketchen, Z.-a. Ren, and Z. X. Zhao. Integer and half-integer flux-quantum transitions in a niobiumiron pnictide loop. *Nature Physics*, 6(4):260–264, February 2010.

[13] D Parker and I I Mazin. Possible phase-sensitive tests of pairing symmetry in pnictide superconductors. *cond-mat.supr-con*, 20375:1–4, 2009.

[14] A. Golubov, A Brinkman, Yukio Tanaka, I. Mazin, and O. Dolgov. Andreev Spectra and Subgap Bound States in Multiband Superconductors. *Physical Review Letters*, 103(7):1–4, August 2009.

[15] M. J. Wang, J. Y. Luo, T. W. Huang, H. H. Chang, T. K. Chen, F. C. Hsu, C. T. Wu, P. M. Wu, A. M. Chang, and M. K. Wu. Crystal Orientation and Thickness Dependence of the Superconducting Transition Temperature of Tetragonal FeSe_{1-x} Thin Films. *Physical Review Letters*, 103(11), September 2009.

[16] E. Bellingeri, I. Pallecchi, R. Buzio, a. Gerbi, D. Marrè, M. R. Cimberle, M. Tropeano, M. Putti, a. Palenzona, S. Kaciulis, and C. Ferdeghini. Critical Temperature Enhancement by Biaxial Compressive Strain in FeSe0.5Te0.5 Thin Films. *Journal of Superconductivity and Novel Magnetism*, 24(1-2):35–41, October 2010.

[17] Shiliang Li, Clarina de la Cruz, Q. Huang, Y. Chen, J. W. Lynn, Jiangping Hu, Yi-Lin Huang, Fong-Chi Hsu, Kuo-Wei Yeh, Maw-Kuen Wu, and Pengcheng Dai. First-order magnetic and structural phase transitions in Fe_{1+y}Se_{x}Te_{1x}. *Physical Review B*, 79(5), February 2009.

[18] Yoshikazu Mizuguchi and Yoshihiko Takano. Superconductivity in PbO-type Fe chalcogenides. *Zeitschrift für Kristallographie*, 226(4):417–434, April 2011.

[19] Alaska Subedi, Lijun Zhang, D. Singh, and M. Du. Density functional study of FeS, FeSe, and FeTe: Electronic structure, magnetism, phonons, and superconductivity. *Physical Review B*, 78(13), October 2008.

[20] C. T. Wu, H. H. Chang, J. Y. Luo, T. J. Chen, F. C. Hsu, T. K. Chen, M. J. Wang, and M. K. Wu. Heterojunction of Fe(Se[sub 1x]Te[sub x]) superconductor on Nb-doped SrTiO[sub 3]. *Applied Physics Letters*, 96(12):122506, 2010.

[21] Ivar Giaever. Energy Gap in Superconductors Measured by Electron Tunneling. *Physical Review Letters*, 5(4):147–148, August 1960.

[22] B Josephson. Possible new effects in superconductive tunnelling. *Physics Letters*, 1(7):251–253, July 1962.

[23] G. Blonder, M. Tinkham, and T. Klapwijk. Transition from metallic to tunneling regimes in superconducting microconstrictions: Excess current, charge imbalance, and supercurrent conversion. *Physical Review B*, 25(7):4515–4532, April 1982.

[24] D Daghero and R S Gonnelli. Probing multiband superconductivity by point-contact spectroscopy. *Superconductor Science and Technology*, 23(4):043001, April 2010.

[25] Satoshi Kashiwaya and Yukio Tanaka. Tunnelling effects on surface bound states in unconventional superconductors. *Reports on Progress in Physics*, 63(10):1641–1724, October 2000.

[26] Michael Cyrot and Davor Pavuna. *Introduction to Superconductivity and high-Tc Materials*. World Scientific Publishing Co. Pte. Ltd., 1992.

[27] Paul Seidel. Josephson effects in iron based superconductors. *Superconductor Science and Technology*, 24(4):043001, April 2011.

[28] A K Geim and K S Novoselov. The rise of graphene. *Nature materials*, 6(3):183–91, March 2007.

[29] Hidenori Hiramatsu, Takayoshi Katase, Toshio Kamiya, and Hideo Hosono. Thin Film Growth and Device Fabrication of Iron-Based Superconductors. pages 1–55, November 2011.

[30] Ya. G. Ponomarev, S. a. Kuzmichev, M. G. Mikheev, M. V. Sudakova, S. N. Tchesnokov, T. E. Shanygina, O. S. Volkova, a. N. Vasiliev, and Th. Wolf. Andreev spectroscopy of FeSe: Evidence for two-gap superconductivity. *Journal of Experimental and Theoretical Physics*, 113(3):459–467, October 2011.

[31] E Bellingeri, R Buzio, A Gerbi, and D Marr. High quality epitaxial FeSe0.5Te0.5 thin films grown on SrTiO3 substrates by pulsed laser deposition. *Superconductor Science and Technology*, 105007, 2009.

[32] Fong-Chi Hsu, Jiu-Yong Luo, Kuo-Wei Yeh, Ta-Kun Chen, Tzu-Wen Huang, Phillip M Wu, Yong-Chi Lee, Yi-Lin Huang, Yan-Yi Chu, Der-Chung Yan, and Maw-Kuen Wu. Superconductivity in the PbO-type structure alpha-FeSe. *Proceedings of the National Academy of Sciences of the United States of America*, 105(38):14262–4, September 2008.

[33] T Geetha Kumary, Dipak Kumar Baisnab, J Janaki, Awadhesh Mani, a T Satya, R M Sarguna, P K Ajikumar, a K Tyagi, and a Bharathi. Superconducting Fe 1+δ Se 1 x Te x thin films: growth, characterization and properties. *Superconductor Science and Technology*, 22(9):095018, September 2009.

[34] Diederik Jekel. Ironing out pnictides. Master's thesis, 2010.

[35] T. M. McQueen, Q. Huang, V. Ksenofontov, C. Felser, Q. Xu, H. Zandbergen, Y. S. Hor, J. Allred, a. J. Williams, D. Qu, J. Checkelsky, N. P. Ong, and R. J. Cava. Extreme sensitivity of superconductivity to stoichiometry in Fe_{1+δ}Se. *Physical Review B*, 79(1):1–7, January 2009.

[36] J B Nelson and D P Riley. An experimental investigation of extrapolation methods in the derivation of accurate unit-cell dimensions of crystals. *Proceedings of the Physical Society*, 57(3):160–177, May 1945.

[37] M.K. Wu, F.C. Hsu, K.W. Yeh, T.W. Huang, J.Y. Luo, M.J. Wang, H.H. Chang, T.K. Chen, S.M. Rao, and B.H. Mok. The development of the superconducting PbO-type β-FeSe and related compounds. *Physica C: Superconductivity*, 469(9-12):340–349, June 2009.

[38] P. L. Paulose, C. S. Yadav, and K. M. Subhedar. Magnetic phase diagram of Fe 1.1 Te 1-x Se x : A comparative study with the stoichiometric superconducting FeTe 1-x Se x system. *EPL (Europhysics Letters)*, 90(2):27011, April 2010.